

Unsupervised domain adaptation for radioisotope identification in gamma spectroscopy

Peter Lalor^{a,*}, Ayush Panigrahy^{a,b}, Alex Hagen^a

^a*Pacific Northwest National Laboratory, Richland, WA 99352 USA*

^b*University of Washington, Seattle, WA 98195 USA*

Abstract

Training machine learning models for radioisotope identification using gamma spectroscopy remains an elusive challenge for many practical applications, largely stemming from the difficulty of acquiring and labeling large, diverse experimental datasets. Simulations can mitigate this challenge, but the accuracy of models trained on simulated data can deteriorate substantially when deployed to an out-of-distribution operational environment. In this study, we demonstrate that unsupervised domain adaptation (UDA) can improve the ability of a model trained on synthetic data to generalize to a new testing domain, provided unlabeled data from the target domain are available. Conventional supervised techniques are unable to utilize this data because the absence of isotope labels precludes defining a supervised classification loss. Instead, we first pretrain a spectral classifier using labeled synthetic data and subsequently leverage unlabeled target data to align the learned feature representations between the source and target domains. We compare a range of different UDA techniques, finding that minimizing the maximum mean discrepancy (MMD) between source and target feature vectors yields the most consistent improvement to testing scores. For instance, using a custom transformer-based neural network, we achieved a testing accuracy of 0.904 ± 0.022 on an experimental LaBr_3 test set after performing unsupervised feature alignment via MMD minimization, compared to 0.754 ± 0.014 before alignment. Overall, our results highlight the potential of using UDA to adapt a radioisotope classifier trained on synthetic data for real-world deployment.

Keywords: Domain Adaptation, Transformer, Neural Network, Gamma Spectroscopy

1. Introduction

Improvements to the current performance of gamma spectroscopy are still sought in many applications, especially those with low signal-to-noise ratios. Very recent papers cite the need for gamma spectroscopic improvements for mobile source search [1], nuclear facility upset detection [2], and national security missions [3] among others. Many current papers, such as those cited above, focus on improvements to the analysis applied to the data obtained from modern hardware, rather than on improvements to the hardware itself. The abundance of detectable photons from natural surroundings interferes with photons emitted from the source of interest across many situations—a problem which cannot be resolved by different hardware. This problem is analogous to standard problems in computer vision (CV) and natural language processing (NLP), where noise (pixels of unimportant objects in CV or stopwords in NLP) interferes with the signal (pixels of

*Corresponding author

Email address: peter.lalor@pnnl.gov

Telephone: (925) 453-1876

the object of interest in CV or key words conveying meaning in NLP). Unlike in CV and NLP, overparameterized machine learning has thus far evaded widespread adoption in the field of gamma spectroscopy. All three fields have challenges associated with training reliable, generalizable, and interpretable models, but the solutions to those challenges from CV and NLP have not been applied to gamma spectroscopy. This is because of the lack of availability of suitable datasets for model training, since collecting and labeling sufficient experimental data is expensive and time-consuming, while relying on synthetic data is inherently limited by the sim-to-real gap [4].

Gamma spectroscopy, especially since the advent of portable spectroscopy detectors in the 1950s [5], is one of the most widely used radiation-detection disciplines. The relative ease of detection of photons compared to neutrons, and their relatively high penetration compared to beta and alpha radiation, lead to the ability to perform standoff detection of radiation sources. This standoff detection is useful in radiation safety, national security, and physical science applications. Additionally, the information conveyed by those photons' energy informs the composition of the source, which is useful in material characterization and forensics applications. Gamma spectrometers themselves have differing efficiency, resolution, and portability characteristics; however, they all display a convolution between the energy of the incident photon across the whole spectrum of detected energy. This is irreducible as it originates in the partial deposition of energy during the interaction of photons with matter, and causes challenges in detection and identification scenarios. Further, many natural materials exhibit photon emission, which leads to an ever-present rate of background photon detection events. These two complicating factors may be mitigated through hardware changes, but require advanced analytics for full resolution.

Thus, advanced analytics like machine learning are not new to the field of gamma spectroscopy. Analysis methods have been developed with increasing levels of sophistication, sometimes preceding other fields. For example, automated peak-finding algorithms were proposed as early as 1967 [6] and deployed in commercial software packages by 2006 [7]; whereas the first algorithm for its computer vision analog, object detection, was not proposed until 2006 [8, 9]. Unconstrained optimization-based curve fitting, the mathematical method which forms the basis for modern neural-network-based machine learning, was developed for the analysis of radiation spectra and reached mainstream (physics) software packages more than 30 years ago [10]. Only recently, and only in terrestrial applications¹, has gamma spectroscopy lagged CV and NLP on its adoption of cutting-edge machine learning techniques.

Machine learning and its applications to CV and NLP changed dramatically in 2012 with the success of AlexNet for classification of images from the ImageNet dataset [12]. The key insight leading to that success was that highly over-parameterized functions called neural networks could be optimized on large datasets to minimize the error on prediction tasks. Since then, parameterization has been a key determinant of machine learning success, and in fact “scaling-laws” which depend on the number of parameters of the model have since emerged [13, 14]. Parameter scaling in gamma spectroscopic analysis has not kept pace with that in CV and NLP. In fact, only some recent publications [4, 15, 16, 17] have embraced the over-parameterized machine learning paradigm.

This slow adoption is likely due to the lack of labeled data in gamma spectroscopy. AlexNet was enabled by the enormous ImageNet dataset, and the aforementioned scaling laws depend on the size of the data as well as the number of parameters in the model. Here again, CV and NLP have developed techniques

¹High-energy physics and cosmology have led CV and NLP on analytics development (e.g., graph neural network architectures in track reconstruction using detection events [11]).

that could be applicable to gamma spectroscopy, notably domain-adaptation and pretraining. Domain-adaptation has been complementary or competitive with pretraining techniques, largely used to supplement models displaying a generalization gap such as CV models trained on natural imagery transferring to overhead imagery [18]. In CV and NLP, self-supervised or semi-supervised pretraining is used to utilize vast amounts of unlabeled data available from scraped internet sources, and is used in most modern Large Language Models and Vision Language Models [19, 20, 21, 22, 23]. Especially with the sim-to-real gap identified in gamma spectroscopy [4], and the lack of consensus over the use of simulated data in other applied data science fields [24, 25], it is important to explore various options for domain adaptation or pretraining-based generalization improvement in gamma spectroscopy. This work presents such a study.

2. Background

2.1. Domain Shift

Domain adaptation for gamma spectroscopy is formalized as follows: we define $P_s(x, y)$ as the joint data-label probability distribution for a gamma spectrum x with label y for the source domain, and likewise $P_t(x, y)$ for the target domain. Our machine learning objective is to train a neural network classifier $h : \mathcal{X} \rightarrow \Delta^K$ to approximate $P_t(y | x)$ – that is, for a given spectrum x from the target domain, we aim to compute the most likely isotopic label y .

Lacking labels from the target domain, we might instead train h using labeled source-domain samples to approximate $P_s(y | x)$ with the hope that $P_s(y | x) \approx P_t(y | x)$ and thus the model trained on source-domain data can be used to classify target-domain spectra. However, in practice this is rarely effective due to the *domain shift* between source, and target domains, which can be broadly categorized in the following types:

Covariate Shift occurs when the underlying distribution of spectra changes between source and target domain even if the mapping from gamma energy spectrum to isotopic labels remains unchanged. For instance, the target domain might contain more shielded examples than the source domain or fewer spectra with low noise. Formally, pure covariate shift occurs when $P_s(x) \neq P_t(x)$ while $P_s(y | x) = P_t(y | x)$.

Prior Shift occurs when the distribution of isotopic labels differs between source and target domain, even if each isotope produces the same distribution of spectra. For instance, the source domain might contain an equal number of every isotope, whereas the target domain contains a class imbalance. Formally, pure prior shift occurs when $P_s(y) \neq P_t(y)$ while $P_s(x | y) = P_t(x | y)$.

Concept Shift occurs when the fundamental relationship between isotopic label and spectral shape is different between source and target domains. For instance, the source and target domain could have a different geometry, background, gain drift, or detector response. Formally, concept shift occurs when $P_s(x | y) \neq P_t(x | y)$. This is the most difficult to fix using UDA techniques, since label-agnostic feature alignment typically requires that concept shift is small.

2.2. Model Architecture

Past literature in gamma spectroscopy implements a range of different machine learning architectures, including multilayer perceptrons (MLPs) [26, 27, 28] and convolutional neural networks (CNNs) [29, 30, 31, 32, 33] to more recent transformer-based neural networks (TBNNs) [34, 4]. We include a summary of each architecture below:

Multilayer Perceptrons represent a gamma spectrum as a 1D list of features and contain one or more hidden layers. Each layer, the features undergo a dense linear transformation followed by a nonlinear activation. MLPs are popular due to their simplicity and flexibility, but lack explicit spatial inductive bias. As a result, MLPs might struggle to learn local structure and are more likely to generalize poorly to spectra with different energy calibrations.

Convolutional Neural Networks implement a sliding 1D convolutional kernel across a gamma spectrum, calculating the dot product between the kernel weights and the local spectrum patch. This process captures spatial structure more efficiently than MLPs, but the locality is limited to nearby energy bins, meaning CNNs can be less effective at capturing long range correlations across a gamma spectrum.

Transformer-based Neural Networks leverage the attention mechanism, first introduced in Ref [19], to compute weights between different regions, or “patches,” of a spectrum. This enables TBNNs to capture long range correlations in a gamma spectrum, such as multiple decays from different nuclear energy levels. However, transformers are more complex to tune and suffer from quadratic scaling with number of spectral patches.

Transformers were first applied to gamma spectroscopy by Ref [34], henceforth TBNN (Li *et al.*). More recent work introduced a more general transformer architecture with learnable patch embeddings and a [CLS] token, among other enhancements [4]. In the present work, we build upon this framework with TBNN-LinEmb and TBNN-NonlinEmb, comparing a single affine projection (i.e., one fully connected layer) to a one-hidden-layer MLP embedder. Furthermore, we use a global average pooling readout instead of a learnable [CLS] token, better matching match spectrum-level classification by aggregating evidence across all channels.

Beyond these architectures, past research has also explored autoencoder-based anomaly detection [17, 15], recurrent neural networks for source identification [17], and custom semi-supervised networks for radioisotope proportion estimation and out-of-distribution identification [35]. Given the more specialized nature of these methods, we focus the architectural analysis of the present work to MLPs, CNNs, and TBNNs.

2.3. Unsupervised Domain Adaptation Methods

In this analysis, we consider the setting where we have access to a labeled *source domain* and an unlabeled *target domain*. The source domain $\mathcal{D}_s = \{(x_i^s, y_i^s)\}_{i=1}^{n_s}$ consists of n_s labeled spectra drawn from $P_s(x, y)$, and the target domain $\mathcal{D}_t = \{x_j^t\}_{j=1}^{n_t}$ consists of n_t spectra drawn from $P_t(x)$ for which labels are not available during training. We first pretrain a *source-only* model using the labeled source domain \mathcal{D}_s , writing our model as the composition $h_{\theta, \phi} = g_{\phi} \circ f_{\theta}$, where $f_{\theta} : \mathcal{X} \rightarrow \mathbb{R}^d$ is the feature extractor and $g_{\phi} : \mathbb{R}^d \rightarrow \Delta^K$ is the classifier. Here, we represent the feature extractor as the entire neural network up to (and including) the penultimate layer, and the classifier as the final dense classification head. We thus write the source-only pretraining objective as follows:

$$\min_{\theta, \phi} \mathcal{L}_{\text{src}}(\theta, \phi) = \frac{1}{n_s} \sum_{i=1}^{n_s} \ell(g_{\phi}(f_{\theta}(x_i^s)), y_i^s) , \quad (1)$$

where $\ell(\cdot, \cdot)$ is the cross-entropy loss. After pretraining a source-only model by minimizing Eq. 1, we consider various UDA methods (Sections 2.3.1–2.3.7) which introduce a modified training objective to encourage alignment between feature distributions $f_{\theta}(\mathcal{D}_s)$ and $f_{\theta}(\mathcal{D}_t)$ using unlabeled target samples from \mathcal{D}_t .

2.3.1. Adversarial Discriminative Domain Adaptation (ADDA)

ADDA [36] trains a new feature extractor f_{θ_t} to produce target-domain features which match the source feature distribution (i.e., $f_{\theta_t}(\mathcal{D}_t) \approx f_{\theta}(\mathcal{D}_s)$). This is accomplished by fixing the source feature extractor and adversarially training a target feature extractor f_{θ_t} and domain discriminator $d_{\psi} : \mathbb{R}^d \rightarrow (0, 1)$. The domain discriminator’s objective is to identify whether a feature distribution originated from a source-domain spectrum (0) or a target-domain spectrum (1), trained via the following:

$$\max_{\psi} \mathbb{E}_{x_s \sim \mathcal{D}_s} [\log(1 - d_{\psi}(f_{\theta}(x_s)))] + \mathbb{E}_{x_t \sim \mathcal{D}_t} [\log d_{\psi}(f_{\theta_t}(x_t))] , \quad (2)$$

while the target feature extractor is trained to fool the discriminator:

$$\min_{\theta_t} \mathbb{E}_{x_t \sim \mathcal{D}_t} [-\log(1 - d_{\psi}(f_{\theta_t}(x_t)))] . \quad (3)$$

The final model is then written as the composition of the source classifier and the target feature extractor: $g_{\phi} \circ f_{\theta_t}$. This approach preserves the source-only model decision boundary while transforming target features to better align with the source domain.

2.3.2. Deep Adaptation Networks (DAN)

DAN [37] adds a term to the supervised source-only loss function to minimize the maximum mean discrepancy (MMD) between the source and target feature vectors $z_s = f_{\theta}(x_s)$ and $z_t = f_{\theta}(x_t)$. MMD is defined as the distance between the source and target feature embeddings in a reproducing kernel Hilbert space (RKHS), calculated using the kernel trick:

$$\text{MMD}^2(z_s, z_t) = \left\| \frac{1}{n_s} \sum_{i=1}^{n_s} \varphi(z_s^i) - \frac{1}{n_t} \sum_{j=1}^{n_t} \varphi(z_t^j) \right\|_{\mathcal{H}}^2 = \frac{1}{n_s^2} \sum_{i,i'} k(z_s^i, z_s^{i'}) + \frac{1}{n_t^2} \sum_{j,j'} k(z_t^j, z_t^{j'}) - \frac{2}{n_s n_t} \sum_{i,j} k(z_s^i, z_t^j) , \quad (4)$$

where k is a positive definite kernel and φ is its feature map. The DAN training objective is thus

$$\min_{\theta, \phi} \mathcal{L}_{\text{src}}(\theta, \phi) + \lambda \text{MMD}^2(z_s, z_t) , \quad (5)$$

where $\lambda \geq 0$ is a tradeoff parameter which balances the contribution of the source-only supervised term with the MMD feature alignment penalty. In our experiments, we compute MMD using a multi-kernel Gaussian radial basis function (RBF), averaging over several kernel bandwidths and omitting diagonal terms. The resulting domain-adapted model thus retains the ability to correctly classify source-domain spectra while simultaneously producing aligned source and target feature vectors, yielding better generalization to the target domain.

2.3.3. Domain Adversarial Neural Networks (DANN)

DANN [38] trains the source feature extractor to learn domain-invariant features. This is accomplished by training a domain discriminator $d_{\psi} : \mathbb{R}^d \rightarrow (0, 1)$ while adversarially updating the feature extractor to fool the discriminator. The min-max objective is thus:

$$\min_{\theta, \phi} \max_{\psi} \mathcal{L}_{\text{src}}(\theta, \phi) - \kappa \mathbb{E}_{x \sim (\mathcal{D}_s \cup \mathcal{D}_t)} [\ell_d(d_{\psi}(f_{\theta}(x)), r(x))] , \quad (6)$$

where $\kappa \geq 0$ is the domain-adversarial strength, $r(x) \in \{0, 1\}$ is the true domain label (0=source, 1=target), and $\ell_d(\cdot, \cdot)$ is the binary cross-entropy loss. In practice, Eq. 6 is optimized using a gradient

reversal layer that multiplies the gradient from the discriminator loss entering the feature extractor by $-\kappa$ during backpropagation. After domain adaptation, the feature extractor produces a domain-agnostic representation and is thus less likely to overfit to features only present in the source domain.

2.3.4. Deep Correlation Alignment (DeepCORAL)

DeepCORAL [39] aligns the second-order statistics of the source and target distributions by minimizing the difference between their covariance matrices. Defining covariances C_s and C_t for minibatch feature matrices $Z_s \in \mathbb{R}^{n_s \times d}$ and $Z_t \in \mathbb{R}^{n_t \times d}$ as:

$$C_s = \frac{1}{n_s - 1} (Z_s - \mathbf{1}\bar{z}_s^\top)^\top (Z_s - \mathbf{1}\bar{z}_s^\top), \quad C_t = \frac{1}{n_t - 1} (Z_t - \mathbf{1}\bar{z}_t^\top)^\top (Z_t - \mathbf{1}\bar{z}_t^\top), \quad (7)$$

we express the CORAL loss as:

$$\mathcal{L}_{\text{CORAL}} = \frac{1}{4d^2} \|C_s - C_t\|_F^2, \quad (8)$$

and subsequently optimize the network via the combined objective:

$$\min_{\theta, \phi} \mathcal{L}_{\text{src}}(\theta, \phi) + \lambda \mathcal{L}_{\text{CORAL}}, \quad (9)$$

where λ is a tradeoff parameter. The result is a simple and lightweight way to align source and target feature distributions.

2.3.5. Deep Joint Optimal Transport (DeepJDOT)

DeepJDOT [40] aligns the *joint* distributions of features and labels using optimal transport (OT). For each minibatch, a pairwise cost is defined as

$$c_{ij}(\theta, \phi) = \alpha \|f_\theta(x_s^i) - f_\theta(x_t^j)\|_2^2 + \beta \ell(g_\phi(f_\theta(x_t^j)), y_s^i), \quad (10)$$

where $\ell(\cdot, \cdot)$ is the cross-entropy loss. The first term in Eq. 10 measures the similarity between samples i and j in feature space, and the second term measures the agreement in label space between the *true* source label y_s and the *predicted* target label $\hat{y}_t = g_\phi(f_\theta(x_t^j))$. In Eq. 10, $\alpha, \beta \geq 0$ are hyperparameters which balance the feature-distance and label-consistency. We then compute a *soft matching* (transport plan) $\gamma \in \mathbb{R}_+^{n_s \times n_t}$ between the n_s source spectra and n_t target spectra by solving the entropic OT problem with uniform marginals using Sinkhorn iterations. We subsequently define the OT loss as follows:

$$\mathcal{L}_{\text{OT}}(\theta, \phi) = \sum_{i=1}^{n_s} \sum_{j=1}^{n_t} \gamma_{ij} c_{ij}(\theta, \phi). \quad (11)$$

Our training objective is thus:

$$\min_{\theta, \phi} \mathcal{L}_{\text{src}}(\theta, \phi) + \lambda \mathcal{L}_{\text{OT}}(\theta, \phi), \quad (12)$$

for a tradeoff parameter λ . Through this OT procedure, we achieve a class aware method of aligning source and target domains.

2.3.6. Mean Teacher

Mean Teacher [41] enforces predictive consistency under noise/augmentations between a *teacher* model and *student* model, where the weights of the teacher are an exponential moving average (EMA) of the student’s weights. For each target spectrum x_t , two stochastic views $x_t^{(s)}$ and $x_t^{(t)}$ are formed by adding Poisson noise to the original spectrum, with an *effective counts* hyperparameter introduced to control the

scale of the noise². We then define a self-supervised consistency loss as the mean squared error between the student’s predictions $g_{\phi_s}(f_{\theta_s}(x_t^{(s)}))$ and the teacher’s predictions $g_{\phi_t}(f_{\theta_t}(x_t^{(t)}))$:

$$\mathcal{L}_{\text{cons}}(\theta_s, \phi_s; \theta_t, \phi_t) = \mathbb{E}_{x_t \sim \mathcal{D}_t} \left[\left\| g_{\phi_s}(f_{\theta_s}(x_t^{(s)})) - g_{\phi_t}(f_{\theta_t}(x_t^{(t)})) \right\|_2^2 \right]. \quad (13)$$

The student parameters are optimized via the combined training objective:

$$\min_{\theta_s, \phi_s} \mathcal{L}_{\text{src}}(\theta_s, \phi_s) + \lambda \mathcal{L}_{\text{cons}}(\theta_s, \phi_s; \theta_t, \phi_t). \quad (14)$$

for a tradeoff parameter λ , and the teacher parameters are updated by EMA:

$$\theta_t \leftarrow \mu \theta_t + (1 - \mu) \theta_s, \quad \phi_t \leftarrow \mu \phi_t + (1 - \mu) \phi_s, \quad (15)$$

where $\mu \in [0, 1)$ is the EMA decay. Mean Teacher encourages stable predictions on target spectra while remaining robust to noise.

2.3.7. Simple Contrastive Learning (SimCLR)

SimCLR [43] performs self-supervised learning by contrasting two stochastic views of the same underlying spectrum. Similar to Mean Teacher, we perform independent Poisson resampling on each target spectrum x_t to generate two views $x_t^{(1)}$ and $x_t^{(2)}$. We subsequently introduce a projection head $q_\omega : \mathbb{R}^d \rightarrow \mathbb{R}^{d'}$ and compute $z_1 = q_\omega(f_{\theta}(x_t^{(1)}))$, $z_2 = q_\omega(f_{\theta}(x_t^{(2)}))$. For a minibatch of m target spectra, we define a contrastive InfoNCE loss as:

$$\mathcal{L}_{\text{NCE}} = \frac{1}{2} (\mathcal{L}_{1 \rightarrow 2} + \mathcal{L}_{2 \rightarrow 1}), \quad \mathcal{L}_{1 \rightarrow 2} = \frac{1}{m} \sum_{i=1}^m -\log \frac{\exp(\text{sim}(z_1^i, z_2^i)/\tau)}{\sum_{j=1}^m \exp(\text{sim}(z_1^i, z_2^j)/\tau)} \quad (16)$$

where $\text{sim}(u, v) = \frac{u^T v}{\|u\| \|v\|}$ is the cosine similarity and $\tau > 0$ is a temperature hyperparameter. The overall training objective is thus:

$$\min_{\theta, \phi, \omega} \mathcal{L}_{\text{src}}(\theta, \phi) + \lambda \mathcal{L}_{\text{NCE}}(\theta, \omega), \quad (17)$$

where $\lambda \geq 0$ is a tradeoff parameter. SimCLR encourages a model to learn augmentation-invariant representations of target spectra while retaining the ability to correctly classify source spectra.

3. Methodology

3.1. Dataset Curation

In this analysis, we consider three domain adaptation scenarios, summarized in Table 1. In the first domain adaptation scenario, *sim-to-sim*, our target domain is simulated in **Geant4**, an open-source Monte Carlo simulation package for modeling the passage of radiation through matter [44, 45]. We simulated high-resolution spectra for 55 radioisotopes by dissolving each isotope in a scintillation cocktail and measuring incoming gamma rays using a high-purity germanium (HPGe) detector placed one meter from the source, mirroring the geometry from Ref. [46]. These template spectra are then mixed, background-added, and

²Alternative data augmentations are possible, such as background addition, detector broadening, peak masking, or gain shift [42]. We selected Poisson resampling to serve as a simple baseline.

Table 1: Summary of the datasets used in this study.

| Scenario | Domain | Acquisition Mode | Isotopic Composition | Number of Isotopes | Size |
|----------------------------------|--------|------------------|----------------------|--------------------|-------------------|
| sim-to-sim (HPGe) | Source | GADRAS | Mixed | 55 | 1.3×10^6 |
| | Target | Geant4 | Mixed | 55 | 1.3×10^6 |
| sim-to-real (LaBr ₃) | Source | GADRAS | Single | 32 | 1.4×10^6 |
| | Target | Experiment | Single | 32 | 15,091 |
| sim-to-real (NaI(Tl)) | Source | GADRAS | Single | 32 | 1.4×10^6 |
| | Target | Experiment | Single | 32 | 10,440 |

Poisson resampled using PyRIID, a python package for gamma spectral synthesis [47]. In the second and third domain adaptation scenarios, our target domain consists of experimental spectra measured using handheld sodium iodide (NaI(Tl)) and lanthanum bromide (LaBr₃) detectors, respectively, measured in standardized source-shield configurations (none, steel, lead, polyethylene). The spectra interpolated onto a uniform 1024-bin energy from from 0 to 3000 keV, and each source belonged to one of 32 isotope classes. In all three domain adaptation scenarios, the isotopic labels of the target domain spectra were masked to imitate a setting where ground truth composition is unknown. The isotopic labels of the validation and testing sets were not masked in order to evaluate the performance of trained models for algorithmic comparison.

For each domain adaptation scenario, we also simulated a corresponding source-domain dataset using GADRAS. GADRAS is a semi-empirical detector response calculation software which couples deterministic attenuation calculations with precomputed response functions to quickly generate synthetic template spectra [48]. These high resolution template spectra are then mixed (sim-to-sim only), background-added, and Poisson resampled using PyRIID to efficiently generate a large dataset for machine learning training. The dataset curation process is described in further detail in our previous research [4].

One significant advantage to including both sim-to-sim and sim-to-real domain adaptation scenarios is the ability to explore the effects of different types of domain shift. The domain gap in the sim-to-sim scenario is dominated by concept shift, as covariate shift and prior shift are both heavily suppressed due to the shared PyRIID data augmentation pipeline. As a result, we expect UDA to be less effective in the sim-to-sim scenario, since concept shift is difficult to solve using unsupervised domain alignment. On the contrary, the sim-to-real scenario represents a more realistic setting in which the domain gap includes contributions from covariate, prior, and concept shift. As such, we expect UDA to offer more quantifiable benefits in the sim-to-real scenarios.

3.2. Model Training

As an input preprocessing step, we applied a variance-stabilizing square-root transform to the raw channel counts, $\tilde{x} = \sqrt{x}$. We subsequently z -score normalized the transformed counts on a per-spectrum basis, $\hat{x} = (\tilde{x} - \mu)/\sigma$, where μ and σ are the mean and standard deviation of \tilde{x} computed across channels for a single spectrum. We found this preprocessing improved training stability, especially for the transformer architectures.

To train the source-only models, we first performed a Bayesian hyperparameter search using the Optuna software package [49]. For each architecture, we performed 100 Bayesian trials with a validation loss search

criterion. For consistency, we used the same architecture hyperparameters across all scenarios (selected as the best source-only parameters from the sim-to-sim dataset), but training hyperparameters (learning rate, batch size, weight decay, dropout) were calculated separately for every run. Once the best hyperparameters were selected, we trained 10 models using different random weight initializations, per-epoch data shuffling, and dropout seeds. This ensemble technique was chosen as a simple form of uncertainty estimation, as the sample standard deviation of metric evaluations across the 10 randomized trials quantifies realistic run-to-run performance fluctuations.

After source-only models were trained, we performed an additional 100 Bayesian trials to determine the best UDA-specific hyperparameters. We performed this search independently for each architecture (Section 2.2) and for each UDA method (Section 2.3). Once the best hyperparameters were selected, we again trained 10 models using different random seeds to estimate uncertainty in model performance. The domain-adapted models and source-only models were paired by using the corresponding source-only model as the initial configuration prior to unsupervised domain alignment. We include a summary of the selected hyperparameters for each domain adaptation scenario across all architectures and UDA methods in Tables A.5–A.13.

4. Results

4.1. Domain Shift Characterization

To illustrate the presence of source-to-target domain shift for each of the domain adaptation scenarios, we computed three domain-gap metrics. First, we trained a linear feature-space domain discriminator $d_\psi : \mathbb{R}^d \rightarrow (0, 1)$ to identify whether a feature vector $z_{s,t} = f_\theta(x_{s,t})$ originated from the source-domain (0) or target-domain (1). We also trained an input-space domain discriminator directly on $x_{s,t}$. We subsequently computed the area under the receiver operating characteristic curve (AUROC) on a held-out test set to quantify how easily each domain discriminator was able to differentiate between source and target domains (AUROC = 0.5 \implies random guessing, AUROC = 1 \implies perfect domain discrimination) [50]. We supplemented this analysis by empirically estimating the MMD (Eq. 4) between source and target ℓ_1 -normalized spectra using an RBF kernel with median heuristic bandwidth (MMD = 0 \implies identical distributions, larger values indicate larger domain gap) [51]. Finally, we defined a class-conditional expected pairwise Wasserstein distance as the average Wasserstein-1 distance $W_1(\cdot, \cdot)$ between random ℓ_1 -normalized spectra for a given isotopic label c [52]. We then compute a custom heuristic R by comparing the source-to-target class-conditional expected pairwise Wasserstein distance to the same distance evaluated within each domain:

$$R(\mathcal{D}_s, \mathcal{D}_t) := \frac{\sum_{c=1}^K \widetilde{W}_{s,t}^{(c)}}{\frac{1}{2} \sum_{c=1}^K (\widetilde{W}_{s,s}^{(c)} + \widetilde{W}_{t,t}^{(c)})}, \quad \widetilde{W}_{s,t}^{(c)} := \mathbb{E}_{\substack{x_s \sim \mathcal{D}_s^c \\ x_t \sim \mathcal{D}_t^c}} [W_1(x_s, x_t)]. \quad (18)$$

Intuitively, we interpret the Wasserstein distance $W_1(\cdot, \cdot)$ between two spectra as the minimal transport cost to morph one spectrum into another, and R as the ratio of between-domain to within-domain spectral dissimilarity. Thus $R = 1 \implies$ consistency between \mathcal{D}_s and \mathcal{D}_t , whereas $R \gg 1 \implies$ substantial dissimilarity. We compute Eq. 18 in the sim-to-sim scenario using single-isotope (one-hot) spectra from both the source and target datasets, since mixed spectra cannot be uniquely assigned to a single class c . For each domain separability metric, we compute a 95% confidence interval (CI) using a stratified bootstrapping approach, and performed statistical significance testing via an approximate bootstrap for AUC (null = 0.5) and R (null = 1) and a permutation test for MMD (null = 0). These results are summarized in table 2, where we see that all three metrics identify a statistically significant source-to-target domain gap across all domain

| Scenario | AUROC (features) | AUROC (inputs) | MMD ² | R |
|----------------------------------|------------------|----------------|------------------|--------------|
| sim-to-sim (HPGe) | [0.993, 0.996] | [0.957, 0.967] | [2.74, 2.93] | [1.36, 1.40] |
| sim-to-real (LaBr ₃) | [0.982, 0.988] | [0.852, 0.874] | [2.26, 2.55] | [1.87, 1.93] |
| sim-to-real (NaI(Tl)) | [0.983, 0.989] | [0.780, 0.808] | [1.30, 2.53] | [1.93, 1.99] |

Table 2: 95% CI for each domain separability metric, indicating a statistically significant domain gap between source and target domains for all domain adaptation scenarios.

adaptation scenarios. This result highlights the importance of leveraging domain adaptation techniques to reduce the impact of domain shift on model generalizability.

4.2. Testing Scores

The results of this analysis are summarized in Table 3, where we compare the performance of different machine learning models on a held-out testing dataset. In the sim-to-real scenarios, we compute the accuracy on the held-out experimental testing dataset as our evaluation metric. In the sim-to-sim scenario, we instead use the APE score [4] as our evaluation metric, calculated via Eq. 19. The APE score provides a simple, bounded $[0, 1]$ agreement metric (0=maximal deviation, 1=perfect reconstruction) to describe how precisely a model reconstructs the mixed isotopic composition of a heterogeneous source.

$$\text{APE}(h_{\theta,\phi}; \mathcal{D}_{\text{test}}) := 1 - \frac{1}{2n_{\text{test}}} \sum_{i=1}^{n_{\text{test}}} \|\hat{y}_i - y_i\|_1, \quad \hat{y}_i := h_{\theta,\phi}(x_i) \in \Delta^K, \quad y_i \in \Delta^K. \quad (19)$$

We observe mixed results in the sim-to-sim scenario. The most consistent performance gain compared to source-only were the DANN models, where the MLP achieved an APE score of 0.649 ± 0.004 (compared to 0.623 ± 0.002 of source-only), TBNN (Li *et al.*) achieved an APE score of 0.690 ± 0.005 (compared to 0.630 ± 0.003 of source-only), TBNN-LinEmb achieved an APE score of 0.691 ± 0.006 (compared to 0.653 ± 0.004 of Source-only), and TBNN-NonlinEmb achieved an APE score of 0.697 ± 0.006 (compared to 0.668 ± 0.005 of source-only). DAN and ADDA yielded similar improvements, although the performance gain was only seen using the three transformer architectures. None of the UDA methods improved performance using a CNN backbone.

In the sim-to-real dataset, we observe a stronger result. Across all architectural backbones, the best UDA model achieves an average classification accuracy improvement of 14.9 percentage points relative to the source-only model. DANN and DAN yielded the strongest average improvement except when using a CNN backbone, in which case DeepCORAL was best. Using the LaBr₃ testing set, the DAN MLP achieved an accuracy of 0.895 ± 0.018 (versus 0.743 ± 0.010 source-only), DeepCORAL CNN achieved 0.937 ± 0.021 (versus 0.800 ± 0.019 source-only), DANN TBNN (Li *et al.*) achieved 0.932 ± 0.022 (versus 0.775 ± 0.010 source-only), DAN TBNN-LinEmb achieved 0.904 ± 0.022 (versus 0.754 ± 0.014 source-only), and DANN TBNN-NonlinEmb achieved 0.934 ± 0.022 (versus 0.765 ± 0.013 baseline).

To statistically support these results, we performed a series of one-sided Wilcoxon signed-rank tests testing the null hypothesis that UDA provides no significant improvement to testing scores compared to the source-only models. We chose a Wilcoxon signed-rank test due to the nature of having paired data (each source-only model was used as the initial configuration for the UDA run) and because the test makes no assumptions regarding the normality of differences. We present the results in Fig. A.14 for all three domain adaptation scenarios. In the sim-to-sim scenario, the domain-adapted models achieve statistically superior

Table 3: Evaluation metric scores on the target-domain test dataset for five different UDA techniques. The “Source-only” row indicates models that were only trained on source-domain data with no domain adaptation step, serving as a baseline. the “Train on Target” row indicates models that were trained on labeled target-domain data, serving as a theoretical best-case scenario. Cell entries are calculated as the mean and sample standard deviation across 10 random trials. The best performing method for each architecture (excluding “Train on Target”) is highlighted in bold.

(a) Scenario: sim-to-sim (HPGe). Cell entries indicate testing APE score

| | MLP | CNN | TBNN (Li <i>et al.</i>) | TBNN-LinEmb | TBNN-NonlinEmb |
|-----------------|----------------------|----------------------|--------------------------|----------------------|----------------------|
| Source-only | 0.623 ± 0.002 | 0.635 ± 0.001 | 0.630 ± 0.003 | 0.653 ± 0.004 | 0.668 ± 0.005 |
| ADDA | 0.604 ± 0.012 | 0.614 ± 0.018 | 0.667 ± 0.007 | 0.678 ± 0.009 | 0.688 ± 0.008 |
| DAN | 0.592 ± 0.004 | 0.607 ± 0.003 | 0.659 ± 0.005 | 0.667 ± 0.004 | 0.691 ± 0.005 |
| DANN | 0.649 ± 0.004 | 0.630 ± 0.012 | 0.690 ± 0.005 | 0.691 ± 0.006 | 0.697 ± 0.006 |
| DeepCORAL | 0.629 ± 0.002 | 0.619 ± 0.012 | 0.641 ± 0.012 | 0.640 ± 0.009 | 0.650 ± 0.006 |
| DeepJDOT | 0.390 ± 0.185 | 0.614 ± 0.005 | 0.631 ± 0.005 | 0.626 ± 0.004 | 0.609 ± 0.011 |
| MeanTeacher | 0.484 ± 0.014 | 0.573 ± 0.009 | 0.589 ± 0.112 | 0.633 ± 0.016 | 0.612 ± 0.026 |
| SimCLR | 0.573 ± 0.005 | 0.605 ± 0.007 | 0.649 ± 0.004 | 0.605 ± 0.006 | 0.648 ± 0.009 |
| Train on Target | 0.896 ± 0.001 | 0.881 ± 0.001 | 0.891 ± 0.001 | 0.895 ± 0.001 | 0.889 ± 0.001 |

(b) Scenario: sim-to-real (LaBr₃). Cell entries indicate testing accuracy

| | MLP | CNN | TBNN (Li <i>et al.</i>) | TBNN-LinEmb | TBNN-NonlinEmb |
|-----------------|----------------------|----------------------|--------------------------|----------------------|----------------------|
| Source-only | 0.743 ± 0.010 | 0.800 ± 0.019 | 0.775 ± 0.010 | 0.754 ± 0.014 | 0.765 ± 0.013 |
| ADDA | 0.807 ± 0.039 | 0.868 ± 0.014 | 0.836 ± 0.036 | 0.821 ± 0.044 | 0.826 ± 0.036 |
| DAN | 0.895 ± 0.018 | 0.841 ± 0.028 | 0.901 ± 0.027 | 0.904 ± 0.022 | 0.878 ± 0.019 |
| DANN | 0.879 ± 0.029 | 0.926 ± 0.016 | 0.932 ± 0.022 | 0.898 ± 0.032 | 0.934 ± 0.022 |
| DeepCORAL | 0.796 ± 0.028 | 0.937 ± 0.021 | 0.853 ± 0.017 | 0.876 ± 0.026 | 0.854 ± 0.024 |
| DeepJDOT | 0.747 ± 0.015 | 0.818 ± 0.020 | 0.800 ± 0.032 | 0.830 ± 0.038 | 0.849 ± 0.030 |
| MeanTeacher | 0.757 ± 0.010 | 0.773 ± 0.032 | 0.866 ± 0.026 | 0.746 ± 0.013 | 0.785 ± 0.021 |
| SimCLR | 0.837 ± 0.014 | 0.869 ± 0.010 | 0.868 ± 0.040 | 0.840 ± 0.032 | 0.853 ± 0.030 |
| Train on Target | 1.000 ± 0.000 | 1.000 ± 0.000 | 1.000 ± 0.000 | 1.000 ± 0.000 | 1.000 ± 0.000 |

(c) Scenario: sim-to-real (NaI(Tl)). Cell entries indicate testing accuracy

| | MLP | CNN | TBNN (Li <i>et al.</i>) | TBNN-LinEmb | TBNN-NonlinEmb |
|-----------------|----------------------|----------------------|--------------------------|----------------------|----------------------|
| Source-only | 0.748 ± 0.011 | 0.818 ± 0.027 | 0.761 ± 0.012 | 0.749 ± 0.018 | 0.742 ± 0.015 |
| ADDA | 0.841 ± 0.034 | 0.847 ± 0.050 | 0.851 ± 0.030 | 0.828 ± 0.035 | 0.739 ± 0.050 |
| DAN | 0.853 ± 0.028 | 0.833 ± 0.034 | 0.933 ± 0.025 | 0.905 ± 0.023 | 0.910 ± 0.029 |
| DANN | 0.888 ± 0.027 | 0.853 ± 0.037 | 0.924 ± 0.022 | 0.898 ± 0.037 | 0.921 ± 0.023 |
| DeepCORAL | 0.797 ± 0.031 | 0.895 ± 0.025 | 0.877 ± 0.027 | 0.881 ± 0.027 | 0.870 ± 0.029 |
| DeepJDOT | 0.802 ± 0.016 | 0.798 ± 0.035 | 0.852 ± 0.030 | 0.875 ± 0.026 | 0.882 ± 0.042 |
| MeanTeacher | 0.739 ± 0.015 | 0.759 ± 0.032 | 0.906 ± 0.018 | 0.776 ± 0.034 | 0.785 ± 0.023 |
| SimCLR | 0.841 ± 0.019 | 0.861 ± 0.026 | 0.930 ± 0.016 | 0.849 ± 0.037 | 0.832 ± 0.041 |
| Train on Target | 1.000 ± 0.000 | 1.000 ± 0.000 | 1.000 ± 0.000 | 1.000 ± 0.000 | 1.000 ± 0.000 |

performance to the source-only models in 13 out of 35 comparisons, while in the sim-to-real scenarios, the domain adapted models achieve statistically superior performance to the source-only models in 30 out of 35 comparisons for the LaBr₃ detector and 27 out of 35 for the NaI(Tl) detector. In particular, using a transformer model (TBNN (Li *et al.*), TBNN-LinEmb, or TBNN-NonlinEmb) with either DAN or DANN for domain adaptation provides a statistically significant improvement over source-only for every comparison across all domain adaptation scenarios.

4.3. Latent Representation Analysis

To interpret the impact of UDA on model behavior, we visualized the extracted feature representations of 2000 source-domain spectra and 2000 target-domain spectra using uniform manifold approximation and projection (UMAP) [53]. We show the results for the sim-to-sim scenario in Fig. 1, where we clearly see that the domain adaptation step results in qualitatively better alignment between the extracted source features and target features. Despite the apparent geometric alignment, our results from Section 4.2 suggest that the improvement to testing APE score is modest (source-only APE = 0.653 ± 0.004 , DAN APE = 0.689 ± 0.005). Given the similarity in mixing procedures when synthesizing the GADRAS and Geant4 datasets (Section 3.1), we interpret this as further evidence that the domain shift in the sim-to-sim scenario is dominated by concept shift. In other words, UDA was able to effectively align the marginal feature distributions $P_s(f_\theta(x))$ and $P_t(f_\theta(x))$, while the class-conditional feature distributions $P_s(f_\theta(x) | y)$ and $P_t(f_\theta(x) | y)$ (i.e., differences in GADRAS and Geant4 detector response for each isotopic mixture) remain separated. We remark that class-conditional alignment is a fundamental limitation of UDA, and thus substantial model improvements would likely necessitate either (i) reducing the concept shift between source and target domains via more faithful GADRAS simulations, or (ii) including some label signal from Geant4 during domain adaptation.

In the sim-to-real LaBr₃ scenario, our observations are almost the opposite. Using the LaBr₃ dataset, we observe in Fig. 2 that UMAP does not drastically improve qualitative feature alignment. We see strong clustering of both synthetic and experimental features, and it is difficult to articulate improved cluster alignment after domain adaptation. Despite this, we observe substantial double-digit improvements to testing accuracy (source-only accuracy = 0.754 ± 0.014 , DAN accuracy = 0.904 ± 0.022). We interpret this as evidence that the domain gap in the sim-to-real scenario does not manifest itself as poor 2D UMAP cluster alignment, but rather in the form of complex, high-dimensional feature incongruence which is relevant to the decision boundary.

4.4. Model Diagnostics

To better understand the performance of our models, we consider a wide range of literature-grounded diagnostic measurements. **Accuracy** measures the fraction of correctly classified testing spectra, and **Negative log-likelihood** [54] reports the average negative log-probability assigned to the true class. **Brier score** [55] measures the mean squared error between predicted probabilities and one-hot labels, and **Expected calibration error** [56] calculates the average absolute difference between accuracy and confidence across probability bins. **Prediction margin mean (p10)** [57] measures the mean (10th) percentile of the log-probability margin between true and best alternative class, and **AUROC (entropy)** evaluates the ability of predictive uncertainty to identify misclassified examples using the area under the receiver operating characteristic of the uncertainty score [58]. **Mean Jacobian norm** measures input sensitivity by calculating the mean squared ℓ_2 norm of the loss gradient with respect to the normalized spectral inputs [59]. Lastly, we construct a k -nearest-neighbor (k -NN) graph of the input spectra and compute the following metrics: [60, 61]

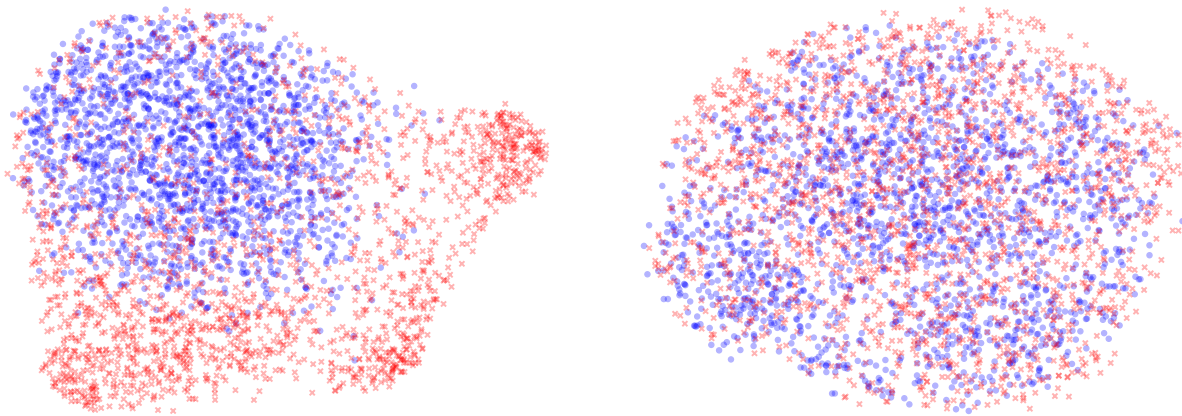


Figure 1: UMAP visualizations of the feature extractor output from 2000 source spectra (blue ‘o’ markers) and 2000 target spectra (red ‘x’ markers) using a TBNN-LinEmb architecture for the sim-to-sim domain adaptation scenario. When only training only on the source dataset (left), the target features show poor alignment with the source features. Using DAN (right), the extracted features show better alignment between the source and target domains.

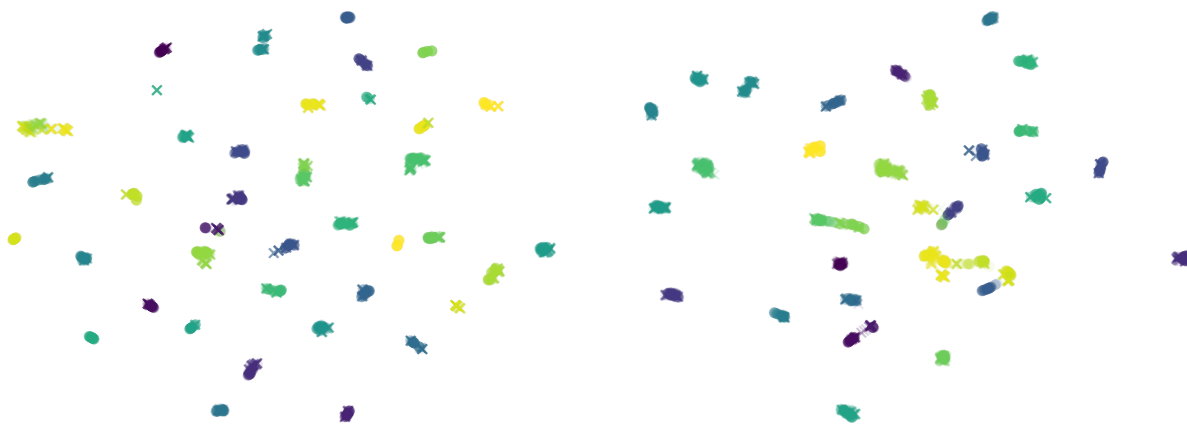


Figure 2: UMAP visualizations of the feature extractor output from 2000 source spectra (‘o’ markers) and 2000 target spectra (‘x’ markers) using a TBNN-LinEmb architecture for the sim-to-real LaBr₃ domain adaptation scenario, with colormap indicating class. Surprisingly, we don’t observe a notice a substantial qualitative difference in clustering quality between the source-only model (left) and the DAN model (right).

Table 4: Comparing the effects of UDA on a variety of diagnostic metrics (\uparrow higher is better, \downarrow lower is better). Source-only and UDA TBNN-LinEmb models are shown for the sim-to-real scenario with a LaBr₃ detector. Entries for the best model are bolded when significant ($p < 0.01$). Overall, UDA provides improvements using a wide variety of metrics beyond classification accuracy.

| Metric | Source-only | DAN | p -value | Dir. | Type |
|---------------------------------|-------------------------------------|-------------------------------------|--------------|--------------|---------------------|
| Accuracy | 0.754 \pm 0.010 | 0.904 \pm 0.021 | 0.002 | \uparrow | Accuracy |
| Negative log-likelihood [54] | 2.840 \pm 0.317 | 0.393 \pm 0.125 | 0.002 | \downarrow | Likelihood / Loss |
| Brier score [55] | 0.455 \pm 0.037 | 0.147 \pm 0.031 | 0.002 | \downarrow | Calibration |
| Expected calibration error [56] | 0.218 \pm 0.025 | 0.044 \pm 0.014 | 0.002 | \downarrow | Calibration |
| Prediction margin (mean) [57] | 6.646 \pm 0.544 | 8.853 \pm 1.055 | 0.002 | \uparrow | Separation / Margin |
| Prediction margin (p10) [57] | -13.543 \pm 1.765 | 0.217 \pm 1.116 | 0.002 | \uparrow | Separation / Margin |
| AUROC (Entropy) [62] | 0.902 \pm 0.036 | 0.940 \pm 0.015 | 0.004 | \uparrow | Uncertainty |
| Mean Jacobian norm [59] | 2.151 \pm 0.498 | 3.348 \pm 2.423 | 0.322 | \downarrow | Sensitivity |
| k -NN TV hard [60, 61] | 0.959 \pm 0.002 | 0.959 \pm 0.003 | 0.515 | \downarrow | Boundary Complexity |
| k -NN prob ℓ_2 [60, 61] | 1.880 \pm 0.026 | 1.839 \pm 0.023 | 0.004 | \downarrow | Smoothness |
| k -NN conf absdiff [60, 61] | 0.028 \pm 0.017 | 0.054 \pm 0.014 | 0.002 | \downarrow | Smoothness |
| k -NN margin absdiff [60, 61] | 7.666 \pm 0.426 | 4.890 \pm 0.649 | 0.002 | \downarrow | Smoothness |

(i) k -NN TV Hard is the fraction of k -NN edges with differing predicted class labels, (ii) k -NN prob ℓ_2 is the mean squared ℓ_2 distance between prediction probability vectors of k -NN neighbors, (iii) k -NN conf absdiff is the mean absolute difference in top-1 confidence between k -NN neighbors, and (iv) k -NN margin absdiff is the mean absolute difference in true-class log-probability margin between k -NN neighbors.

We show the results in Table 4 for a TBNN-LinEmb model in the sim-to-real LaBr₃ dataset using the trained source-only and DAN models. To test for statistical significance using a two-sided Wilcoxon signed-rank test, testing the null hypothesis that there is no difference in diagnostic metric value between the two models. Overall, we find that the DAN model wins in 9 out of 12 metrics, the source-only model in 1 out of 12, and 2 out of 12 considered statistically insignificant. Overall, we present statistical evidence that UDA improves model performance in a range of calibration, separation, uncertainty, and input-space smoothness metrics.

4.5. Model Interpretability

To gain insight into our models’ decision-making process, we used SHapley Additive exPlanations (SHAP) [16, 63] to compute per-region feature attributions. For a given gamma spectrum, SHAP produces an *explanation vector* of SHAP values by assigning an attribution to each spectral region, indicating how that region shifts the model predicted isotope probability relative to a baseline. The SHAP values are computed by repeatedly masking random regions of a spectrum, evaluating the model on the perturbed spectrum, and then averaging each region’s marginal contribution. In this context, we mask a region by replacing the counts in the selected bins with values obtained by log-linear interpolation between the region’s endpoints. Regions with large positive (negative) SHAP values increase (decrease) the predicted probability for a given isotope, while values near zero indicate little average effect.

In Fig. 3, we use a colorbar to overlay the computed SHAP values on top of a LaBr₃ ⁴⁰K gamma spectrum using a source-only model (left) and a domain-adapted model (right). SHAP reveals that the source-only model identifies the LaBr₃ detector’s intrinsic 32 keV Ba K-shell X-ray peak as salient, confusing it with the 40 keV X-rays emitted from electron capture on ¹⁵²Eu. On the contrary, the DAN model correctly learns to

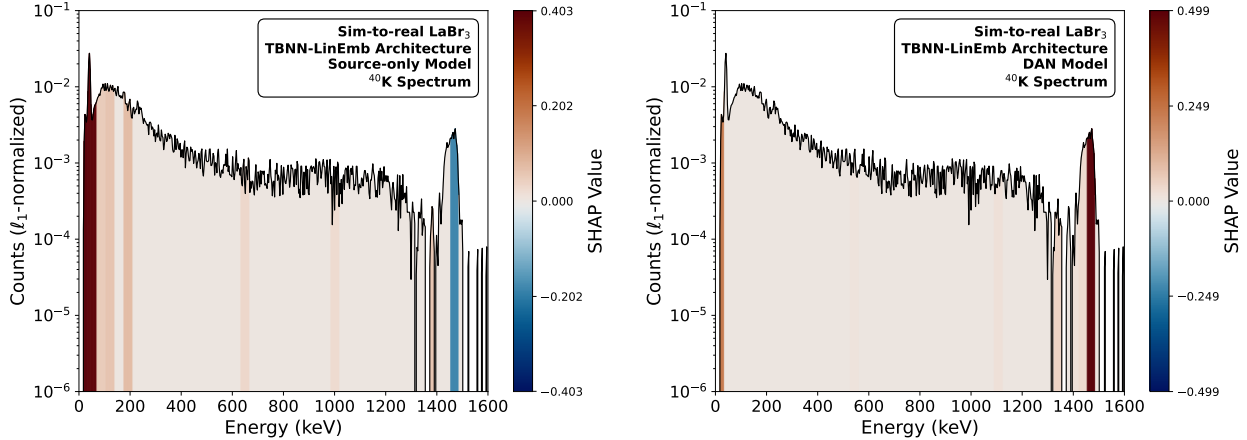


Figure 3: SHAP explanations for a ^{40}K spectrum using a source-only model (left) and a DAN model (right). The source-only model only identifies the LaBr₃ detector’s intrinsic 32 keV X-ray peak as salient, whereas the DAN model instead highlights the correct 1460 keV line.

ignore the 32 keV characteristic X-ray and instead focus on the 1460 keV peak from ^{40}K . As a result, the DAN model achieves a ^{40}K classification accuracy of 83%, compared to 17% from the source-only model.

5. Conclusions

This study uses UDA to improve the performance of radioisotope identification models in scenarios where target-domain data is available but lacks ground-truth labels. We compared several different UDA methods (ADDA, DAN, DANN, DeepCORAL, DeepJDOT) and architectural backbones (MLP, CNN, TBNN), finding that UDA provides a statistically significant improvement to testing scores in both sim-to-sim and sim-to-real scenarios. These improvements were more pronounced in the sim-to-real studies, where we found that DAN and DANN reliably yielded double digit improvements to testing accuracy across the MLP and TBNN model families. For instance, the DAN TBNN-LinEmb achieves a testing accuracy of 0.904 ± 0.022 on the experimental LaBr₃ dataset, compared to 0.754 ± 0.014 of the source-only model. The improvements in the sim-to-sim scenario were less pronounced but still statistically significant, validating the hypothesis that domain shift in sim-to-sim was more challenging to resolve using unsupervised feature alignment.

We support the conclusions of this study using a range of quantitative diagnostic metrics and qualitative explainability and interpretability techniques. In addition to testing accuracy, DAN achieves improved likelihood, calibration, and margin compared to the source-only model on the sim-to-real LaBr₃ dataset. Furthermore, SHAP analysis reveals that the DAN model is able to more consistently highlight salient spectral features and less likely to overfit to spurious high-count, low-energy peaks. Overall, we find that UDA is a practical tool for adapting synthetic-pretrained ML methods for radioisotope identification tasks in operational scenarios where unlabeled experimental datasets are available.

6. Data Availability

Datasets and model training code can be found at <https://github.com/pnnl/gamma-adapt/> for the sim-to-sim domain adaptation scenario. Due to data sensitivity, the code, data, and best models for the sim-to-real dataset are not available for public release.

7. Acknowledgements

This research was supported by the Laboratory Directed Research and Development Program at Pacific Northwest National Laboratory, a multiprogram national laboratory operated by Battelle for the U.S. Department of Energy under contract DE-AC05-76RLO1830. Peter Lalor is grateful for the support of the Linus Pauling Distinguished Postdoctoral Fellowship. The authors would like to acknowledge Tyler Morrow and Brian Archambault for their useful suggestions and feedback. The authors declare no conflict of interest.

References

- [1] D. Breitenmoser, A. Stabilini, M. M. Kasprzak, S. Mayer, Quantitative mobile gamma-ray spectrometry through Bayesian inference (Jan. 2026). [arXiv:2512.18769](#), doi:10.48550/arXiv.2512.18769.
- [2] P. R. Fernández, C. Svinth, A. Hagen, Improvement of Nuclide Detection through Graph Spectroscopic Analysis Framework and its Application to Nuclear Facility Upset Detection (Jun. 2025). [arXiv:2506.16522](#), doi:10.48550/arXiv.2506.16522.
- [3] S. E. Labov, K. E. Nelson, C. M. Mattoon, N. J. McFerran, M. H. Pham, L. Her, J. S. Brzosko, S. Ray, D. Howarth, A. W. Dubrawski, Improving operational performance using machine learning analysis of Radiation Portal Monitor measurements, *Nuclear Instruments and Methods in Physics Research Section A: Accelerators, Spectrometers, Detectors and Associated Equipment* 1072 (2025) 170123. doi:10.1016/j.nima.2024.170123.
- [4] P. Lalor, H. Adams, A. Hagen, Sim-to-real supervised domain adaptation for radioisotope identification, *Nuclear Instruments and Methods in Physics Research Section A: Accelerators, Spectrometers, Detectors and Associated Equipment* 1083 (2026) 171159. doi:<https://doi.org/10.1016/j.nima.2025.171159>.
URL <https://www.sciencedirect.com/science/article/pii/S0168900225009611>
- [5] G. F. Knoll, *Radiation Detection and Measurement*, 4th Edition, Wiley, Hoboken, NJ, 2010.
- [6] M. A. Mariscotti, A method for automatic identification of peaks in the presence of background and its application to spectrum analysis, *Nuclear Instruments and Methods* 50 (2) (1967) 309–320. doi:10.1016/0029-554X(67)90058-4.
- [7] Genie 2000 Operations Manual.
- [8] P. Viola, M. Jones, Rapid object detection using a boosted cascade of simple features, in: *Proceedings of the 2001 IEEE Computer Society Conference on Computer Vision and Pattern Recognition. CVPR 2001*, Vol. 1, 2001, pp. I–I. doi:10.1109/CVPR.2001.990517.
- [9] Z. Zou, K. Chen, Z. Shi, Y. Guo, J. Ye, Object Detection in 20 Years: A Survey (Jan. 2023). [arXiv:1905.05055](#), doi:10.48550/arXiv.1905.05055.
- [10] F. James, *MINUIT: Function Minimization and Error Analysis Reference Manual*, CERN Program Library Long Writeup D506, Conseil Européen pour la Recherche Nucléaire (CERN), Geneva (1994).
- [11] L. Reuter, G. D. Pietro, S. Stefkova, T. Ferber, V. Bertacchi, G. Casarosa, L. Corona, P. Ecker, A. Glazov, Y. Han, M. Laurenza, T. Lueck, L. Massaccesi, S. Mondal, B. Scavino, S. Spataro, C. Wessel, L. Zani, End-to-End Multi-Track Reconstruction using Graph Neural Networks at Belle II (Nov. 2024). [arXiv:2411.13596](#), doi:10.48550/arXiv.2411.13596.
- [12] A. Krizhevsky, I. Sutskever, G. E. Hinton, ImageNet Classification with Deep Convolutional Neural Networks, in: *Advances in Neural Information Processing Systems*, Vol. 25, Curran Associates, Inc., 2012.
- [13] J. Hestness, S. Narang, N. Ardalani, G. Diamos, H. Jun, H. Kianinejad, M. M. A. Patwary, Y. Yang, Y. Zhou, Deep Learning Scaling is Predictable, Empirically (Dec. 2017). [arXiv:1712.00409](#), doi:10.48550/arXiv.1712.00409.
- [14] I. Alabdulmohsin, B. Neyshabur, X. Zhai, Revisiting Neural Scaling Laws in Language and Vision (Nov. 2022). [arXiv:2209.06640](#), doi:10.48550/arXiv.2209.06640.
- [15] J. M. Ghawaly, A. D. Nicholson, D. E. Archer, M. J. Willis, I. Garishvili, B. Longmire, A. J. Rowe, I. R. Stewart, M. T. Cook, Characterization of the autoencoder radiation anomaly detection (arad) model, *Engineering Applications of Artificial Intelligence* 111 (2022) 104761. doi:10.1016/j.engappai.2022.

104761.

URL <https://www.sciencedirect.com/science/article/pii/S0952197622000550>

- [16] M. S. Bandstra, J. C. Curtis, J. M. Ghawaly, Jr, A. C. Jones, T. H. Y. Joshi, Explaining machine-learning models for gamma-ray detection and identification, *PLOS ONE* 18 (6) (2023) 1–21. doi:10.1371/journal.pone.0286829.
URL <https://doi.org/10.1371/journal.pone.0286829>
- [17] K. J. Bilton, T. H. Y. Joshi, M. S. Bandstra, J. C. Curtis, D. Hellfeld, K. Vetter, Neural network approaches for mobile spectroscopic gamma-ray source detection, *Journal of Nuclear Engineering* 2 (2) (2021) 190–206. doi:10.3390/jne2020018.
URL <https://www.mdpi.com/2673-4362/2/2/18>
- [18] A. Farahani, S. Voghoei, K. Rasheed, H. R. Arabnia, A Brief Review of Domain Adaptation (Oct. 2020). arXiv:2010.03978, doi:10.48550/arXiv.2010.03978.
- [19] A. Vaswani, N. Shazeer, N. Parmar, J. Uszkoreit, L. Jones, A. N. Gomez, Ł. Kaiser, I. Polosukhin, Attention is all you need, in: *Advances in Neural Information Processing Systems*, Vol. 2017-Decem, Neural information processing systems foundation, 2017, pp. 5999–6009. arXiv:1706.03762.
- [20] T. B. Brown, B. Mann, N. Ryder, M. Subbiah, J. Kaplan, P. Dhariwal, A. Neelakantan, P. Shyam, G. Sastry, A. Askell, S. Agarwal, A. Herbert-Voss, G. Krueger, T. Henighan, R. Child, A. Ramesh, D. M. Ziegler, J. Wu, C. Winter, C. Hesse, M. Chen, E. Sigler, M. Litwin, S. Gray, B. Chess, J. Clark, C. Berner, S. McCandlish, A. Radford, I. Sutskever, D. Amodei, Language Models are Few-Shot Learners (Jul. 2020). arXiv:2005.14165, doi:10.48550/arXiv.2005.14165.
- [21] A. Radford, K. Narasimhan, T. Salimans, I. Sutskever, Improving Language Understanding by Generative Pre-Training.
- [22] A. Radford, J. Wu, R. Child, D. Luan, D. Amodei, I. Sutskever, Language Models are Unsupervised Multitask Learners.
- [23] J. Devlin, M.-W. Chang, K. Lee, K. Toutanova, BERT: Pre-training of Deep Bidirectional Transformers for Language Understanding (May 2019). arXiv:1810.04805, doi:10.48550/arXiv.1810.04805.
- [24] C. Ly, W. Frazier, A. Olsen, I. Schwerdt, L. W. McDonald, A. Hagen, Improving microstructures segmentation via pretraining with synthetic data, *Computational Materials Science* 249 (2025) 113639. doi:10.1016/j.commatsci.2024.113639.
- [25] A. Jain, A. Montanari, E. Sasoglu, Scaling laws for learning with real and surrogate data, *Advances in Neural Information Processing Systems* 37 (2024) 110246–110289.
- [26] P. Olmos, J. Diaz, J. Perez, P. Gomez, V. Rodellar, P. Aguayo, A. Bru, G. Garcia-Belmonte, J. de Pablos, A new approach to automatic radiation spectrum analysis, *IEEE Transactions on Nuclear Science* 38 (4) (1991) 971–975. doi:10.1109/23.83860.
- [27] P. Olmos, J. Diaz, J. Perez, G. Garcia-Belmonte, P. Gomez, V. Rodellar, Application of neural network techniques in gamma spectroscopy, *Nuclear Instruments and Methods in Physics Research Section A: Accelerators, Spectrometers, Detectors and Associated Equipment* 312 (1) (1992) 167–173. doi:[https://doi.org/10.1016/0168-9002\(92\)90148-W](https://doi.org/10.1016/0168-9002(92)90148-W).
URL <https://www.sciencedirect.com/science/article/pii/016890029290148W>
- [28] M. Kamuda, J. Zhao, K. Huff, A comparison of machine learning methods for automated gamma-ray spectroscopy, *Nuclear Instruments and Methods in Physics Research Section A: Accelerators, Spectrometers, Detectors and Associated Equipment* 954 (2020) 161385, symposium on Radiation Measurements and Applications XVII. doi:10.1016/j.nima.2018.10.063.

- URL <https://www.sciencedirect.com/science/article/pii/S0168900218313779>
- [29] D. Liang, P. Gong, X. Tang, P. Wang, L. Gao, Z. Wang, R. Zhang, Rapid nuclide identification algorithm based on convolutional neural network, *Annals of Nuclear Energy* 133 (2019) 483–490. doi:10.1016/j.anucene.2019.05.051.
URL <https://www.sciencedirect.com/science/article/pii/S0306454919303044>
- [30] E. T. Moore, W. P. Ford, E. J. Hague, J. Turk, An application of cnns to time sequenced one dimensional data in radiation detection (2019). arXiv:1908.10887.
URL <https://arxiv.org/abs/1908.10887>
- [31] E. T. Moore, J. L. Turk, W. P. Ford, N. J. Hoteling, L. S. McLean, Transfer learning in automated gamma spectral identification (2020). arXiv:2003.10524.
URL <https://arxiv.org/abs/2003.10524>
- [32] G. Daniel, F. Ceraudo, O. Limousin, D. Maier, A. Meuris, Automatic and real-time identification of radionuclides in gamma-ray spectra: A new method based on convolutional neural network trained with synthetic data set, *IEEE Transactions on Nuclear Science* 67 (4) (2020) 644–653. doi:10.1109/TNS.2020.2969703.
- [33] N. Barradas, A. Vieira, M. Felizardo, M. Matos, Nuclide identification of radioactive sources from gamma spectra using artificial neural networks, *Radiation Physics and Chemistry* 232 (2025) 112692. doi:<https://doi.org/10.1016/j.radphyschem.2025.112692>.
URL <https://www.sciencedirect.com/science/article/pii/S0969806X25001847>
- [34] F. Li, C.-Y. Luo, Y.-Z. Wen, S. Lv, F. Cheng, G.-Q. Zeng, J.-F. Jiang, B.-H. Li, A nuclide identification method of γ spectrum and model building based on the transformer, *Nuclear Science and Techniques* 36 (1) (2024) 7. doi:10.1007/s41365-024-01564-5.
URL <https://doi.org/10.1007/s41365-024-01564-5>
- [35] A. Van Omen, T. Morrow, C. Scott, E. Leonard, Multilabel proportion prediction and out-of-distribution detection on gamma spectra of short-lived fission products, *Annals of Nuclear Energy* 208 (2024) 110777. doi:10.1016/j.anucene.2024.110777.
URL <https://www.sciencedirect.com/science/article/pii/S0306454924004407>
- [36] E. Tzeng, J. Hoffman, K. Saenko, T. Darrell, Adversarial discriminative domain adaptation (2017). arXiv:1702.05464.
URL <https://arxiv.org/abs/1702.05464>
- [37] M. Long, Y. Cao, J. Wang, M. I. Jordan, Learning transferable features with deep adaptation networks (2015). arXiv:1502.02791.
URL <https://arxiv.org/abs/1502.02791>
- [38] Y. Ganin, E. Ustinova, H. Ajakan, P. Germain, H. Larochelle, F. Laviolette, M. Marchand, V. Lempitsky, Domain-adversarial training of neural networks (2016). arXiv:1505.07818.
URL <https://arxiv.org/abs/1505.07818>
- [39] B. Sun, K. Saenko, Deep coral: Correlation alignment for deep domain adaptation (2016). arXiv:1607.01719.
URL <https://arxiv.org/abs/1607.01719>
- [40] B. B. Damodaran, B. Kellenberger, R. Flamary, D. Tuia, N. Courty, Deepjdot: Deep joint distribution optimal transport for unsupervised domain adaptation (2018). arXiv:1803.10081.
URL <https://arxiv.org/abs/1803.10081>
- [41] A. Tarvainen, H. Valpola, Mean teachers are better role models: Weight-averaged consistency targets

- improve semi-supervised deep learning results (2018). [arXiv:1703.01780](https://arxiv.org/abs/1703.01780).
URL <https://arxiv.org/abs/1703.01780>
- [42] J. Stomps, P. Wilson, K. Dayman, M. Willis, J. Ghawaly, D. Archer, Data augmentations for nuclear feature extraction in semi-supervised contrastive machine learning, in: Proceedings of the INMM/ESARDA Joint Annual Meeting 2023, Institute of Nuclear Materials Management (INMM), Vienna, Austria, 2023.
URL <https://resources.inmm.org/annual-meeting-proceedings/data-augmentations-nuclear-feature-extra>
- [43] T. Chen, S. Kornblith, M. Norouzi, G. Hinton, A simple framework for contrastive learning of visual representations (2020). [arXiv:2002.05709](https://arxiv.org/abs/2002.05709).
URL <https://arxiv.org/abs/2002.05709>
- [44] J. Allison, K. Amako, J. Apostolakis, P. Arce, M. Asai, T. Aso, E. Bagli, A. Bagulya, S. Banerjee, G. Barrand, B. Beck, A. Bogdanov, D. Brandt, J. Brown, H. Burkhardt, P. Canal, D. Cano-Ott, S. Chauvie, K. Cho, G. Cirrone, G. Cooperman, M. Cortés-Giraldo, G. Cosmo, G. Cuttone, G. Depaola, L. Desorgher, X. Dong, A. Dotti, V. Elvira, G. Folger, Z. Francis, A. Galoyan, L. Garnier, M. Gayer, K. Genser, V. Grichine, S. Guatelli, P. Guèye, P. Gumplinger, A. Howard, I. Hřivnáčová, S. Hwang, S. Incerti, A. Ivanchenko, V. Ivanchenko, F. Jones, S. Jun, P. Kaitaniemi, N. Karakatsanis, M. Karamitros, M. Kelsey, A. Kimura, T. Koi, H. Kurashige, A. Lechner, S. Lee, F. Longo, M. Maire, D. Mancusi, A. Mantero, E. Mendoza, B. Morgan, K. Murakami, T. Nikitina, L. Pandola, P. Paprocki, J. Perl, I. Petrović, M. Pia, W. Pokorski, J. Quesada, M. Raine, M. Reis, A. Ribon, A. Ristić Fira, F. Romano, G. Russo, G. Santin, T. Sasaki, D. Sawkey, J. Shin, I. Strakovsky, A. Taborda, S. Tanaka, B. Tomé, T. Toshito, H. Tran, P. Truscott, L. Urban, V. Uzhinsky, J. Verbeke, M. Verderi, B. Wendt, H. Wenzel, D. Wright, D. Wright, T. Yamashita, J. Yarba, H. Yoshida, Recent developments in geant4, Nuclear Instruments and Methods in Physics Research Section A: Accelerators, Spectrometers, Detectors and Associated Equipment 835 (2016) 186–225. doi:10.1016/j.nima.2016.06.125.
URL <https://www.sciencedirect.com/science/article/pii/S0168900216306957>
- [45] B. Archambault, B. Pierson, B. Loer, G4ares-geant4 advanced radio-emission simulation framework, available from <https://gitlab.pnnl.gov/ares/g4ares> [accessed November 20, 2024] (2023).
- [46] B. D. Pierson, B. C. Archambault, L. R. Greenwood, M. M. Haney, M. G. Cantaloub, A. R. Hagen, S. M. Herman, N. E. Uhnak, J. M. Bowen, J. H. Estrada, Alpha/beta-gated gamma–gamma spectroscopy of mixed fission products for trace analysis, Journal of Radioanalytical and Nuclear Chemistry 331 (12) (2022) 5453–5467. doi:10.1007/s10967-022-08606-5.
URL <https://doi.org/10.1007/s10967-022-08606-5>
- [47] T. Morrow, N. Price, T. McGuire, Pyriid v.2.0.0, [Computer Software] (apr 2021). doi:10.11578/dc.20221017.2.
URL <https://doi.org/10.11578/dc.20221017.2>
- [48] S. M. Horne, G. G. Thoreson, L. A. Theisen, D. J. Mitchell, L. Harding, W. A. Amai, Gadras-drf 18.6 user’s manual (5 2016). doi:10.2172/1431293.
URL <https://www.osti.gov/biblio/1431293>
- [49] T. Akiba, S. Sano, T. Yanase, T. Ohta, M. Koyama, Optuna: A next-generation hyperparameter optimization framework, in: Proceedings of the 25th ACM SIGKDD International Conference on Knowledge Discovery & Data Mining, KDD ’19, Association for Computing Machinery, New York, NY, USA, 2019, p. 2623–2631. doi:10.1145/3292500.3330701.
URL <https://doi.org/10.1145/3292500.3330701>

- [50] S. Ben-David, J. Blitzer, K. Crammer, A. Kulesza, F. Pereira, J. Vaughan, A theory of learning from different domains, *Machine Learning* 79 (2010) 151–175. doi:10.1007/s10994-009-5152-4.
- [51] A. Gretton, K. M. Borgwardt, M. J. Rasch, B. Schölkopf, A. Smola, A kernel two-sample test, *J. Mach. Learn. Res.* 13 (null) (2012) 723–773.
- [52] G. Peyré, M. Cuturi, Computational optimal transport, *Found. Trends Mach. Learn.* 11 (5–6) (2019) 355–607. doi:10.1561/22000000073.
URL <https://doi.org/10.1561/22000000073>
- [53] L. McInnes, J. Healy, J. Melville, Umap: Uniform manifold approximation and projection for dimension reduction (2020). arXiv:1802.03426.
URL <https://arxiv.org/abs/1802.03426>
- [54] K. P. Murphy, *Machine learning: a probabilistic perspective*, MIT press, 2012.
- [55] W. B. Glenn, et al., Verification of forecasts expressed in terms of probability, *Monthly weather review* 78 (1) (1950) 1–3.
- [56] C. Guo, G. Pleiss, Y. Sun, K. Q. Weinberger, On calibration of modern neural networks, in: *International conference on machine learning*, PMLR, 2017, pp. 1321–1330.
- [57] P. Bartlett, Y. Freund, W. S. Lee, R. E. Schapire, Boosting the margin: A new explanation for the effectiveness of voting methods, *The annals of statistics* 26 (5) (1998) 1651–1686.
- [58] D. Hendrycks, K. Gimpel, A baseline for detecting misclassified and out-of-distribution examples in neural networks (2018). arXiv:1610.02136.
URL <https://arxiv.org/abs/1610.02136>
- [59] I. J. Goodfellow, J. Shlens, C. Szegedy, Explaining and harnessing adversarial examples, arXiv preprint arXiv:1412.6572 (2014).
- [60] M. Belkin, P. Niyogi, V. Sindhwani, Manifold regularization: A geometric framework for learning from labeled and unlabeled examples, *Journal of Machine Learning Research* 7 (85) (2006) 2399–2434.
URL <http://jmlr.org/papers/v7/belkin06a.html>
- [61] X. Zhu, Z. Ghahramani, J. D. Lafferty, Semi-supervised learning using gaussian fields and harmonic functions, in: *Proceedings of the 20th International conference on Machine learning (ICML-03)*, 2003, pp. 912–919.
- [62] C. E. Shannon, A mathematical theory of communication, *The Bell system technical journal* 27 (3) (1948) 379–423.
- [63] S. Lundberg, S.-I. Lee, A unified approach to interpreting model predictions (2017). arXiv:1705.07874.
URL <https://arxiv.org/abs/1705.07874>

Appendix A. Supplementary Materials

Table A.5: Source-only architecture hyperparameter optimization summary for MLP, CNN, TBNN (Li *et al.*), and TBNN-LinEmb, and TBNN-NonlinEmb architectures. The table details the search spaces and best-performing hyperparameter values obtained via a Bayesian search using the source dataset from the sim-to-sim scenario. The best-performing hyperparameters are used for all models across different scenarios in this study.

| Architecture | Parameter | Search Space | Best run |
|--------------------------|--------------------------|--------------|----------|
| MLP | Num Dense Layers | {1, 4} | 2 |
| | Dense1 Hidden Units | {512, 8192} | 8192 |
| | Dense2 Hidden Units | {256, 4096} | 4096 |
| CNN | Num Convolutional Layers | {1, 2} | 1 |
| | Conv Filters | {16, 256} | 32 |
| | Conv Kernel Size | {3, 9} | 5 |
| | Num Dense Layers | {1, 2} | 2 |
| | Dense1 Hidden Units | {512, 8192} | 8192 |
| | Dense2 Hidden Units | {256, 4096} | 4096 |
| TBNN (Li <i>et al.</i>) | Num Attention Blocks | {1, 8} | 4 |
| | Num Heads | {1, 8} | 4 |
| | FF Dimension | {64, 8192} | 2048 |
| TBNN-LinEmb | Embedding Dimension | {8, 1024} | 256 |
| | Num Attention Blocks | {1, 5} | 5 |
| | Num Heads | {1, 8} | 2 |
| | FF Dimension | {16, 16384} | 512 |
| | Patch Size | {16, 64} | 64 |
| TBNN-NonLinEmb | Embedder Hidden Units | {8, 2048} | 512 |
| | Embedding Dimension | {8, 1024} | 512 |
| | Num Attention Blocks | {1, 5} | 3 |
| | Num Heads | {1, 8} | 4 |
| | FF Dimension | {16, 16384} | 1024 |
| | Patch Size | {16, 64} | 64 |

Table A.6: Source-only training hyperparameter optimization summary for MLP, CNN, TBNN (Li *et al.*), and TBNN-LinEmb, and TBNN-NonlinEmb architectures. The table details the search spaces and best-performing hyperparameter values obtained via a Bayesian search using the source dataset.

| Architecture | Parameter | Search Space | Best run | | |
|--------------------------|---------------|--------------|--------------------|----------------------------------|------------------------|
| | | | sim-to-sim HPGe | sim-to-real LaBr ₃ | sim-to-real NaI(Tl) |
| MLP | Learning rate | {1e-5, 2e-3} | 4.60e-5 | 1.80e-3 | 1.32e-3 |
| | Batch size | {32, 512} | 256 | 512 | 256 |
| | Weight decay | {1e-7, 1e-3} | 1.54e-5 | 1.96e-6 | 1.21e-4 |
| | Dropout | {0.0, 0.4} | 0.230 | 0.394 | 0.224 |
| CNN | Learning rate | {1e-5, 2e-3} | 6.45e-5 | 5.54e-5 | 1.89e-4 |
| | Batch size | {32, 512} | 128 | 128 | 256 |
| | Weight decay | {1e-7, 1e-3} | 1.03e-5 | 1.07e-7 | 5.25e-5 |
| | Dropout | {0.0, 0.4} | 0.0714 | 0.375 | 0.386 |
| TBNN (Li <i>et al.</i>) | Learning rate | {1e-5, 2e-3} | 1.65e-3 | 1.28e-3 | 2.99e-4 |
| | Batch size | {32, 512} | 512 | 512 | 256 |
| | Weight decay | {1e-7, 1e-3} | 9.06e-6 | 2.66e-5 | 5.39e-5 |
| | Dropout | {0.0, 0.1} | 3.31e-5 | 0.0349 | 0.0623 |
| TBNN-LinEmb | Learning rate | {1e-5, 2e-3} | 2.75e-4 | 1.01e-4 | 1.54e-4 |
| | Batch size | {32, 512} | 256 | 512 | 512 |
| | Weight decay | {1e-7, 1e-3} | 1.23e-7 | 2.56e-6 | 8.89e-7 |
| | Dropout | {0.0, 0.1} | 2.90e-3 | 0.0413 | 0.0737 |
| TBNN-NonLinEmb | Learning rate | {1e-5, 2e-3} | 1.94e-4 | 2.27e-5 | 1.32e-4 |
| | Batch size | {32, 512} | 256 | 256 | 512 |
| | Weight decay | {1e-7, 1e-3} | 2.47e-7 | 6.49e-4 | 3.39e-4 |
| | Dropout | {0.0, 0.1} | 3.24e-4 | 0.0479 | 0.0947 |

Table A.7: ADDA hyperparameter optimization summary for MLP, CNN, TBNN (Li *et al.*), and TBNN-LinEmb, and TBNN-NonlinEmb architectures. The table details the search spaces and best-performing hyperparameter values obtained via a Bayesian search.

| Architecture | Parameter | Search Space | Best run | | |
|--------------------------|----------------------------|--------------|--------------------|----------------------------------|------------------------|
| | | | sim-to-sim HPGe | sim-to-real LaBr ₃ | sim-to-real NaI(Tl) |
| MLP | FE learning rate | {1e-8, 1e-2} | 5.22e-7 | 1.67e-4 | 2.18e-4 |
| | DD learning rate | {1e-8, 1e-2} | 4.42e-6 | 3.87e-6 | 5.03e-6 |
| | Batch size | {64, 512} | 128 | 128 | 64 |
| | Weight decay | {1e-7, 1e-3} | 2.67e-5 | 2.35e-6 | 8.33e-4 |
| | Dropout | {0.0, 0.4} | 0.376 | 0.282 | 0.156 |
| | Num discriminator layers | {1, 2} | 2 | 2 | 1 |
| | Discriminator dense1 units | {512, 4096} | 1024 | 4096 | 4096 |
| | Discriminator dense2 units | {256, 2048} | 512 | 2048 | N/A |
| CNN | FE learning rate | {1e-8, 1e-2} | 1.24e-7 | 2.62e-5 | 4.47e-5 |
| | DD learning rate | {1e-8, 1e-2} | 6.75e-7 | 2.39e-4 | 3.88e-3 |
| | Batch size | {64, 512} | 64 | 64 | 64 |
| | Weight decay | {1e-7, 1e-3} | 6.62e-5 | 1.18e-5 | 2.31e-5 |
| | Dropout | {0.0, 0.4} | 0.363 | 0.291 | 0.352 |
| | Num discriminator layers | {1, 2} | 2 | 1 | 1 |
| | Discriminator dense1 units | {512, 4096} | 2048 | 2048 | 4096 |
| | Discriminator dense2 units | {256, 2048} | 1024 | N/A | N/A |
| TBNN (Li <i>et al.</i>) | FE learning rate | {1e-8, 1e-2} | 2.57e-6 | 5.28e-5 | 2.81e-5 |
| | DD learning rate | {1e-8, 1e-2} | 2.96e-6 | 8.43e-6 | 2.76e-6 |
| | Batch size | {64, 512} | 256 | 128 | 512 |
| | Weight decay | {1e-7, 1e-3} | 1.18e-5 | 9.73e-4 | 4.95e-7 |
| | Dropout | {0.0, 0.4} | 0.022 | 0.0561 | 0.103 |
| | Num discriminator layers | {1, 2} | 2 | 1 | 1 |
| | Discriminator dense1 units | {512, 4096} | 2048 | 1024 | 4096 |
| | Discriminator dense2 units | {256, 2048} | 1024 | N/A | N/A |
| TBNN-LinEmb | FE learning rate | {1e-8, 1e-2} | 1.15e-6 | 3.24e-6 | 7.33e-6 |
| | DD learning rate | {1e-8, 1e-2} | 3.50e-5 | 9.38e-6 | 8.65e-6 |
| | Batch size | {64, 512} | 256 | 128 | 64 |
| | Weight decay | {1e-7, 1e-3} | 1.07e-7 | 4.88e-4 | 1.57e-7 |
| | Dropout | {0.0, 0.4} | 0.093 | 0.221 | 0.203 |
| | Num discriminator layers | {1, 2} | 1 | 2 | 2 |
| | Discriminator dense1 units | {512, 4096} | 2048 | 1024 | 4096 |
| | Discriminator dense2 units | {256, 2048} | N/A | 512 | 2048 |
| TBNN-NonLinEmb | FE learning rate | {1e-8, 1e-2} | 9.20e-7 | 5.15e-6 | 4.70e-6 |
| | DD learning rate | {1e-8, 1e-2} | 8.29e-6 | 1.95e-5 | 2.23e-6 |
| | Batch size | {64, 512} | 128 | 64 | 512 |
| | Weight decay | {1e-7, 1e-3} | 2.31e-7 | 2.88e-7 | 1.36e-5 |
| | Dropout | {0.0, 0.4} | 0.0147 | 0.196 | 0.0285 |
| | Num discriminator layers | {1, 2} | 1 | 2 | 1 |
| | Discriminator dense1 units | {512, 4096} | 512 | 4096 | 2048 |
| | Discriminator dense2 units | {256, 2048} | N/A | 2048 | N/A |

Table A.8: Same as table A.7, but using DAN.

| Architecture | Parameter | Search Space | Best run | | |
|--------------------------|--------------------|--------------|--------------------|----------------------------------|------------------------|
| | | | sim-to-sim HPGe | sim-to-real LaBr ₃ | sim-to-real NaI(Tl) |
| MLP | Learning rate | {1e-7, 1e-3} | 1.30e-5 | 9.72e-4 | 6.84e-4 |
| | Batch size | {64, 512} | 512 | 256 | 128 |
| | Weight decay | {1e-7, 1e-3} | 7.89e-6 | 8.15e-5 | 6.24e-6 |
| | Dropout | {0.0, 0.4} | 0.0225 | 1.10e-3 | 3.71e-3 |
| | Tradeoff parameter | {1e-1, 1e4} | 4846 | 871 | 1100 |
| | RBF bandwidth | {1e-1, 1e2} | 78.0 | 6.22 | 16.9 |
| | Number of kernels | {3, 15} | 11 | 15 | 11 |
| CNN | Learning rate | {1e-7, 1e-3} | 4.47e-5 | 9.82e-4 | 3.25e-5 |
| | Batch size | {64, 512} | 128 | 256 | 64 |
| | Weight decay | {1e-7, 1e-3} | 1.49e-4 | 2.65e-7 | 5.79e-4 |
| | Dropout | {0.0, 0.4} | 8.06e-3 | 0.177 | 0.0227 |
| | Tradeoff parameter | {1e-1, 1e4} | 340 | 261 | 82.1 |
| | RBF bandwidth | {1e-1, 1e2} | 5.44 | 0.572 | 80.4 |
| | Number of kernels | {3, 15} | 13 | 7 | 15 |
| TBNN (Li <i>et al.</i>) | Learning rate | {1e-7, 1e-3} | 6.98e-5 | 7.47e-4 | 7.74e-4 |
| | Batch size | {64, 512} | 256 | 64 | 256 |
| | Weight decay | {1e-7, 1e-3} | 7.84e-7 | 2.68e-5 | 3.30e-6 |
| | Dropout | {0.0, 0.4} | 0.0621 | 0.0198 | 0.213 |
| | Tradeoff parameter | {1e-1, 1e4} | 1781 | 286 | 159 |
| | RBF bandwidth | {1e-1, 1e2} | 3.51 | 32.1 | 26.3 |
| | Number of kernels | {3, 15} | 15 | 13 | 15 |
| TBNN-LinEmb | Learning rate | {1e-7, 1e-3} | 3.19e-5 | 3.92e-4 | 4.08e-4 |
| | Batch size | {64, 512} | 512 | 512 | 256 |
| | Weight decay | {1e-7, 1e-3} | 4.48e-5 | 5.19e-7 | 1.38e-5 |
| | Dropout | {0.0, 0.4} | 0.132 | 0.165 | 0.272 |
| | Tradeoff parameter | {1e-1, 1e4} | 136 | 381 | 185 |
| | RBF bandwidth | {1e-1, 1e2} | 33.0 | 1.91 | 0.844 |
| | Number of kernels | {3, 15} | 11 | 9 | 15 |
| TBNN-NonLinEmb | Learning rate | {1e-7, 1e-3} | 7.77e-6 | 4.44e-4 | 4.70e-4 |
| | Batch size | {64, 512} | 128 | 512 | 512 |
| | Weight decay | {1e-7, 1e-3} | 5.86e-4 | 9.19e-4 | 7.75e-5 |
| | Dropout | {0.0, 0.4} | 0.0776 | 0.337 | 0.0733 |
| | Tradeoff parameter | {1e-1, 1e4} | 26.3 | 440 | 168 |
| | RBF bandwidth | {1e-1, 1e2} | 3.78 | 26.9 | 42.1 |
| | Number of kernels | {3, 15} | 9 | 3 | 11 |

Table A.9: Same as table A.7, but using DANN.

| Architecture | Parameter | Search Space | Best run | | |
|--------------------------|------------------|--------------|--------------------|----------------------------------|------------------------|
| | | | sim-to-sim HPGe | sim-to-real LaBr ₃ | sim-to-real NaI(Tl) |
| MLP | FE learning rate | {1e-8, 1e-2} | 1.31e-6 | 1.05e-3 | 3.69e-4 |
| | DD learning rate | {1e-8, 1e-2} | 1.06e-5 | 1.52e-4 | 1.17e-4 |
| | Batch size | {64, 512} | 256 | 512 | 512 |
| | Weight decay | {1e-7, 1e-3} | 1.26e-7 | 2.06e-4 | 1.12e-6 |
| | Dropout | {0.0, 0.4} | 0.0588 | 0.046 | 8.29e-3 |
| | Num GRL layers | {1, 2} | 1 | 2 | 2 |
| | GRL dense1 units | {64, 2048} | 1024 | 2048 | 64 |
| | GRL dense2 units | {32, 1024} | N/A | 1024 | 32 |
| | GRL κ | {0.0, 1.0} | 0.643 | 0.634 | 0.777 |
| CNN | FE learning rate | {1e-8, 1e-2} | 1.79e-3 | 1.24e-5 | 4.62e-5 |
| | DD learning rate | {1e-8, 1e-2} | 1.83e-4 | 4.29e-5 | 4.30e-4 |
| | Batch size | {64, 512} | 64 | 512 | 256 |
| | Weight decay | {1e-7, 1e-3} | 8.55e-7 | 4.61e-4 | 1.06e-5 |
| | Dropout | {0.0, 0.4} | 0.386 | 9.40e-3 | 0.223 |
| | Num GRL layers | {1, 2} | 2 | 2 | 1 |
| | GRL dense1 units | {64, 2048} | 2048 | 2048 | 64 |
| | GRL dense2 units | {32, 1024} | 1024 | 1024 | N/A |
| | GRL κ | {0.0, 1.0} | 0.372 | 0.665 | 0.491 |
| TBNN (Li <i>et al.</i>) | FE learning rate | {1e-8, 1e-2} | 4.24e-5 | 1.27e-3 | 2.21e-3 |
| | DD learning rate | {1e-8, 1e-2} | 7.52e-5 | 3.89e-4 | 4.52e-4 |
| | Batch size | {64, 512} | 64 | 128 | 512 |
| | Weight decay | {1e-7, 1e-3} | 2.93e-6 | 1.25e-5 | 2.41e-6 |
| | Dropout | {0.0, 0.4} | 0.0283 | 0.0215 | 0.328 |
| | Num GRL layers | {1, 2} | 1 | 2 | 2 |
| | GRL dense1 units | {64, 2048} | 128 | 512 | 256 |
| | GRL dense2 units | {32, 1024} | N/A | 256 | 128 |
| | GRL κ | {0.0, 1.0} | 0.573 | 0.89 | 0.117 |
| TBNN-LinEmb | FE learning rate | {1e-8, 1e-2} | 4.81e-5 | 1.01e-4 | 2.31e-4 |
| | DD learning rate | {1e-8, 1e-2} | 4.41e-5 | 2.80e-4 | 1.62e-3 |
| | Learning rate | {1e-7, 1e-3} | 4.61e-5 | 1.68e-4 | 6.12e-4 |
| | Batch size | {64, 512} | 512 | 256 | 256 |
| | Weight decay | {1e-7, 1e-3} | 1.99e-5 | 1.29e-4 | 5.97e-7 |
| | Dropout | {0.0, 0.4} | 0.139 | 0.0126 | 0.0986 |
| | Num GRL layers | {1, 2} | 2 | 2 | 2 |
| | GRL dense1 units | {64, 2048} | 1024 | 2048 | 512 |
| | GRL dense2 units | {32, 1024} | 512 | 1024 | 256 |
| | GRL κ | {0.0, 1.0} | 0.0676 | 0.665 | 0.813 |
| TBNN-NonLinEmb | FE learning rate | {1e-8, 1e-2} | 5.41e-5 | 5.21e-5 | 3.26e-4 |
| | DD learning rate | {1e-8, 1e-2} | 2.76e-5 | 2.37e-4 | 8.01e-4 |
| | Batch size | {64, 512} | 512 | 64 | 512 |
| | Weight decay | {1e-7, 1e-3} | 1.54e-7 | 2.72e-5 | 1.18e-4 |
| | Dropout | {0.0, 0.4} | 0.193 | 0.162 | 0.123 |
| | Num GRL layers | {1, 2} | 2 | 2 | 2 |
| | GRL dense1 units | {64, 2048} | 1024 | 1024 | 2048 |
| | GRL dense2 units | {32, 1024} | 512 | 512 | 1024 |
| | GRL κ | {0.0, 1.0} | 0.207 | 0.456 | 0.718 |

Table A.10: Same as table A.7, but using DeepCORAL.

| Architecture | Parameter | Search Space | Best run | | |
|--------------------------|--------------------|--------------|--------------------|----------------------------------|------------------------|
| | | | sim-to-sim HPGe | sim-to-real LaBr ₃ | sim-to-real NaI(Tl) |
| MLP | Learning rate | {1e-7, 1e-3} | 5.36e-5 | 8.95e-4 | 9.41e-4 |
| | Batch size | {64, 512} | 256 | 512 | 128 |
| | Weight decay | {1e-7, 1e-3} | 1.35e-5 | 1.19e-6 | 6.11e-7 |
| | Dropout | {0.0, 0.4} | 0.0441 | 8.24e-3 | 0.0839 |
| | Tradeoff parameter | {1e-1, 1e10} | 1.47e8 | 1.20e9 | 5.77e7 |
| CNN | Learning rate | {1e-7, 1e-3} | 2.27e-5 | 7.44e-4 | 7.13e-4 |
| | Batch size | {64, 512} | 512 | 512 | 512 |
| | Weight decay | {1e-7, 1e-3} | 5.22e-7 | 4.21e-4 | 7.84e-5 |
| | Dropout | {0.0, 0.4} | 0.039 | 0.0887 | 0.0634 |
| | Tradeoff parameter | {1e-1, 1e10} | 2.48e5 | 3.61e3 | 715 |
| TBNN (Li <i>et al.</i>) | Learning rate | {1e-7, 1e-3} | 4.57e-4 | 7.82e-4 | 9.98e-4 |
| | Batch size | {64, 512} | 512 | 128 | 128 |
| | Weight decay | {1e-7, 1e-3} | 2.59e-7 | 4.02e-4 | 1.83e-7 |
| | Dropout | {0.0, 0.4} | 4.82e-3 | 0.289 | 0.119 |
| | Tradeoff parameter | {1e-1, 1e10} | 1.72e8 | 1.16e5 | 4.39e3 |
| TBNN-LinEmb | Learning rate | {1e-7, 1e-3} | 1.41e-4 | 7.16e-4 | 4.75e-4 |
| | Batch size | {64, 512} | 512 | 512 | 512 |
| | Weight decay | {1e-7, 1e-3} | 1.29e-7 | 1.21e-7 | 4.10e-6 |
| | Dropout | {0.0, 0.4} | 0.0724 | 0.228 | 0.0166 |
| | Tradeoff parameter | {1e-1, 1e10} | 4.02e4 | 3.31e3 | 863 |
| TBNN-NonLinEmb | Learning rate | {1e-7, 1e-3} | 1.24e-4 | 8.16e-4 | 5.21e-4 |
| | Batch size | {64, 512} | 512 | 512 | 512 |
| | Weight decay | {1e-7, 1e-3} | 7.84e-7 | 9.77e-6 | 2.31e-5 |
| | Dropout | {0.0, 0.4} | 0.131 | 0.0632 | 0.221 |
| | Tradeoff parameter | {1e-1, 1e10} | 1.85e4 | 3.78e3 | 3.65e3 |

Table A.11: Same as table A.7, but using DeepJDOT.

| Architecture | Parameter | Search Space | Best run | | |
|--------------------------|-------------------------|--------------|--------------------|----------------------------------|------------------------|
| | | | sim-to-sim HPGe | sim-to-real LaBr ₃ | sim-to-real NaI(Tl) |
| MLP | Learning rate | {1e-7, 1e-3} | 1.51e-6 | 7.15e-4 | 7.24e-4 |
| | Batch size | {64, 512} | 64 | 512 | 256 |
| | Weight decay | {1e-7, 1e-3} | 4.52e-5 | 5.23e-6 | 9.17e-4 |
| | Dropout | {0.0, 0.4} | 0.275 | 0.177 | 0.216 |
| | Tradeoff parameter | {1e-2, 1e2} | 0.0109 | 0.0204 | 0.0107 |
| | Sinkhorn regularization | {1e-2, 1e1} | 7.81 | 4.36 | 7.57 |
| | Sinkhorn iterations | {5, 30} | 19 | 24 | 17 |
| | JDOT α | {1e-2, 1e1} | 0.0238 | 0.205 | 1.14 |
| | JDOT β | {0.0, 2.0} | 1.35 | 0.222 | 1.41 |
| CNN | Learning rate | {1e-7, 1e-3} | 8.07e-4 | 3.42e-4 | 6.13e-5 |
| | Batch size | {64, 512} | 256 | 64 | 512 |
| | Weight decay | {1e-7, 1e-3} | 2.63e-5 | 1.51e-5 | 1.73e-4 |
| | Dropout | {0.0, 0.4} | 0.0157 | 0.173 | 0.0443 |
| | Tradeoff parameter | {1e-2, 1e2} | 0.135 | 1.28 | 0.0456 |
| | Sinkhorn regularization | {1e-2, 1e1} | 0.0229 | 0.0117 | 9.39 |
| | Sinkhorn iterations | {5, 30} | 12 | 5 | 18 |
| | JDOT α | {1e-2, 1e1} | 0.0227 | 0.174 | 0.0362 |
| | JDOT β | {0.0, 2.0} | 0.636 | 0.354 | 0.961 |
| TBNN (Li <i>et al.</i>) | Learning rate | {1e-7, 1e-3} | 1.41e-5 | 2.25e-4 | 8.75e-4 |
| | Batch size | {64, 512} | 256 | 128 | 128 |
| | Weight decay | {1e-7, 1e-3} | 5.84e-6 | 4.17e-5 | 1.56e-5 |
| | Dropout | {0.0, 0.4} | 0.0579 | 0.106 | 0.111 |
| | Tradeoff parameter | {1e-2, 1e2} | 0.0299 | 5.06 | 0.730 |
| | Sinkhorn regularization | {1e-2, 1e1} | 6.78 | 0.242 | 0.0132 |
| | Sinkhorn iterations | {5, 30} | 23 | 19 | 5 |
| | JDOT α | {1e-2, 1e1} | 0.0238 | 0.0126 | 0.0549 |
| | JDOT β | {0.0, 2.0} | 0.826 | 1.12 | 0.413 |
| TBNN-LinEmb | Learning rate | {1e-7, 1e-3} | 3.38e-6 | 3.33e-5 | 1.94e-4 |
| | Batch size | {64, 512} | 128 | 64 | 128 |
| | Weight decay | {1e-7, 1e-3} | 7.73e-6 | 7.67e-5 | 4.45e-4 |
| | Dropout | {0.0, 0.4} | 0.167 | 0.231 | 0.376 |
| | Tradeoff parameter | {1e-2, 1e2} | 0.0215 | 68.9 | 0.0533 |
| | Sinkhorn regularization | {1e-2, 1e1} | 0.516 | 0.707 | 2.11 |
| | Sinkhorn iterations | {5, 30} | 22 | 28 | 6 |
| | JDOT α | {1e-2, 1e1} | 0.348 | 0.0119 | 0.239 |
| | JDOT β | {0.0, 2.0} | 1.90 | 1.01 | 1.89 |
| TBNN-NonLinEmb | Learning rate | {1e-7, 1e-3} | 1.57e-5 | 3.17e-6 | 1.52e-4 |
| | Batch size | {64, 512} | 256 | 64 | 256 |
| | Weight decay | {1e-7, 1e-3} | 7.26e-5 | 6.04e-5 | 1.80e-5 |
| | Dropout | {0.0, 0.4} | 0.218 | 0.260 | 0.0582 |
| | Tradeoff parameter | {1e-2, 1e2} | 0.495 | 0.0562 | 0.0134 |
| | Sinkhorn regularization | {1e-2, 1e1} | 0.866 | 1.38 | 1.63 |
| | Sinkhorn iterations | {5, 30} | 16 | 24 | 6 |
| | JDOT α | {1e-2, 1e1} | 4.73 | 0.0424 | 0.0902 |
| | JDOT β | {0.0, 2.0} | 1.93 | 1.42 | 0.794 |

Table A.12: Same as table A.7, but using Mean Teacher.

| Architecture | Parameter | Search Space | Best run | | |
|--------------------------|--------------------|---------------|--------------------|----------------------------------|------------------------|
| | | | sim-to-sim HPGe | sim-to-real LaBr ₃ | sim-to-real NaI(Tl) |
| MLP | Learning rate | {1e-7, 1e-3} | 9.06e-4 | 5.36e-4 | 8.24e-4 |
| | Batch size | {64, 512} | 512 | 64 | 64 |
| | Weight decay | {1e-7, 1e-3} | 7.45e-7 | 6.91e-6 | 6.83e-6 |
| | Dropout | {0.0, 0.4} | 0.0229 | 0.183 | 0.121 |
| | Tradeoff parameter | {1e-2, 1e3} | 689 | 430 | 273 |
| | EMA decay | {0.95, 0.999} | 0.9969 | 0.9559 | 0.9520 |
| | Effective counts | {1e2, 5e4} | 3.91e4 | 213 | 169 |
| CNN | Learning rate | {1e-7, 1e-3} | 7.57e-4 | 2.42e-4 | 7.16e-4 |
| | Batch size | {64, 512} | 64 | 256 | 128 |
| | Weight decay | {1e-7, 1e-3} | 7.36e-4 | 7.51e-7 | 2.51e-5 |
| | Dropout | {0.0, 0.4} | 0.365 | 0.0831 | 0.146 |
| | Tradeoff parameter | {1e-2, 1e3} | 10.1 | 818 | 722 |
| | EMA decay | {0.95, 0.999} | 0.9928 | 0.9634 | 0.9504 |
| | Effective counts | {1e2, 5e4} | 4.22e3 | 257 | 124 |
| TBNN (Li <i>et al.</i>) | Learning rate | {1e-7, 1e-3} | 3.36e-4 | 9.62e-4 | 7.52e-4 |
| | Batch size | {64, 512} | 256 | 64 | 128 |
| | Weight decay | {1e-7, 1e-3} | 8.01e-5 | 2.77e-4 | 1.84e-4 |
| | Dropout | {0.0, 0.4} | 0.0461 | 0.363 | 0.283 |
| | Tradeoff parameter | {1e-2, 1e3} | 63.4 | 3.02 | 0.558 |
| | EMA decay | {0.95, 0.999} | 0.9723 | 0.9523 | 0.9783 |
| | Effective counts | {1e2, 5e4} | 1.44e4 | 3.12e4 | 6.29e3 |
| TBNN-LinEmb | Learning rate | {1e-7, 1e-3} | 8.51e-4 | 9.26e-4 | 8.64e-4 |
| | Batch size | {64, 512} | 512 | 128 | 64 |
| | Weight decay | {1e-7, 1e-3} | 7.26e-6 | 7.13e-7 | 1.22e-4 |
| | Dropout | {0.0, 0.4} | 0.0878 | 0.0149 | 9.67e-3 |
| | Tradeoff parameter | {1e-2, 1e3} | 8.58 | 322 | 3.83 |
| | EMA decay | {0.95, 0.999} | 0.9814 | 0.9942 | 0.9526 |
| | Effective counts | {1e2, 5e4} | 3.92e4 | 395 | 224 |
| TBNN-NonLinEmb | Learning rate | {1e-7, 1e-3} | 7.93e-4 | 8.15e-4 | 5.58e-4 |
| | Batch size | {64, 512} | 128 | 64 | 64 |
| | Weight decay | {1e-7, 1e-3} | 1.76e-7 | 2.03e-6 | 2.36e-6 |
| | Dropout | {0.0, 0.4} | 0.0317 | 0.0454 | 0.0108 |
| | Tradeoff parameter | {1e-2, 1e3} | 3.76 | 2.17 | 1.92 |
| | EMA decay | {0.95, 0.999} | 0.9956 | 0.9591 | 0.9571 |
| | Effective counts | {1e2, 5e4} | 5.39e3 | 172 | 336 |

Table A.13: Same as table A.7, but using SimCLR.

| Architecture | Parameter | Search Space | Best run | | |
|--------------------------|--------------------|--------------|--------------------|----------------------------------|------------------------|
| | | | sim-to-sim HPGe | sim-to-real LaBr ₃ | sim-to-real NaI(Tl) |
| MLP | Learning rate | {1e-7, 1e-3} | 5.85e-4 | 3.21e-4 | 6.21e-4 |
| | Batch size | {64, 512} | 128 | 128 | 128 |
| | Weight decay | {1e-7, 1e-3} | 2.00e-5 | 1.99e-4 | 5.92e-7 |
| | Dropout | {0.0, 0.4} | 0.124 | 0.101 | 0.311 |
| | Tradeoff parameter | {1e-2, 1e3} | 670 | 41.2 | 74.8 |
| | Temperature | {1e-2, 0.5} | 0.0918 | 0.499 | 0.491 |
| | Projection layers | {1, 3} | 1 | 1 | 1 |
| | Projection width | {64, 1024} | 128 | 256 | 256 |
| | Effective counts | {1e2, 1e5} | 3.02e4 | 4.69e3 | 1.84e3 |
| CNN | Learning rate | {1e-7, 1e-3} | 1.40e-4 | 5.82e-6 | 9.08e-4 |
| | Batch size | {64, 512} | 512 | 256 | 256 |
| | Weight decay | {1e-7, 1e-3} | 4.98e-7 | 6.44e-5 | 4.37e-6 |
| | Dropout | {0.0, 0.4} | 0.0990 | 0.262 | 0.103 |
| | Tradeoff parameter | {1e-2, 1e3} | 95.7 | 472 | 2.63 |
| | Temperature | {1e-2, 0.5} | 0.0664 | 0.173 | 0.449 |
| | Projection layers | {1, 3} | 1 | 2 | 1 |
| | Projection width | {64, 1024} | 1024 | 1024 | 1024 |
| | Effective counts | {1e2, 1e5} | 7.42e4 | 1.38e4 | 8.40e4 |
| TBNN (Li <i>et al.</i>) | Learning rate | {1e-7, 1e-3} | 6.80e-4 | 8.78e-4 | 7.01e-4 |
| | Batch size | {64, 512} | 512 | 64 | 128 |
| | Weight decay | {1e-7, 1e-3} | 5.44e-7 | 4.21e-7 | 5.65e-7 |
| | Dropout | {0.0, 0.4} | 0.0500 | 0.283 | 0.266 |
| | Tradeoff parameter | {1e-2, 1e3} | 0.151 | 362 | 1.61 |
| | Temperature | {1e-2, 0.5} | 0.0364 | 0.154 | 0.0821 |
| | Projection layers | {1, 3} | 2 | 1 | 1 |
| | Projection width | {64, 1024} | 128 | 128 | 128 |
| | Effective counts | {1e2, 1e5} | 2.29e4 | 5.98e3 | 7.16e4 |
| TBNN-LinEmb | Learning rate | {1e-7, 1e-3} | 9.58e-5 | 9.24e-4 | 4.58e-4 |
| | Batch size | {64, 512} | 128 | 128 | 64 |
| | Weight decay | {1e-7, 1e-3} | 3.62e-7 | 1.61e-6 | 7.28e-6 |
| | Dropout | {0.0, 0.4} | 0.208 | 0.159 | 0.142 |
| | Tradeoff parameter | {1e-2, 1e3} | 0.418 | 1.55 | 278 |
| | Temperature | {1e-2, 0.5} | 0.0469 | 0.201 | 0.443 |
| | Projection layers | {1, 3} | 1 | 1 | 2 |
| | Projection width | {64, 1024} | 1024 | 64 | 128 |
| | Effective counts | {1e2, 1e5} | 169 | 3.97e3 | 3.93e4 |
| TBNN-NonLinEmb | Learning rate | {1e-7, 1e-3} | 9.06e-4 | 5.22e-5 | 7.50e-4 |
| | Batch size | {64, 512} | 512 | 64 | 128 |
| | Weight decay | {1e-7, 1e-3} | 3.58e-7 | 3.57e-6 | 9.72e-7 |
| | Dropout | {0.0, 0.4} | 0.0785 | 0.166 | 0.207 |
| | Tradeoff parameter | {1e-2, 1e3} | 36.8 | 13.2 | 177 |
| | Temperature | {1e-2, 0.5} | 0.0738 | 0.430 | 0.495 |
| | Projection layers | {1, 3} | 1 | 1 | 3 |
| | Projection width | {64, 1024} | 64 | 256 | 1024 |
| | Effective counts | {1e2, 1e5} | 6.87e3 | 1.34e4 | 1.29e4 |

Table A.14: Calculated p -values from a one-sided Wilcoxon signed-rank test, testing the null hypothesis that UDA provides no improvement over the source-only baseline model. p -values below a significance threshold of 0.01 are bolded, indicating statistically significant improvement.

(a) Scenario: sim-to-sim (HPGe). Statistical significance tests compare testing APE score (UDA > source-only).

| | MLP | CNN | TBNN (Li <i>et al.</i>) | TBNN-LinEmb | TBNN-NonlinEmb |
|-------------|--------------|-------|--------------------------|--------------|----------------|
| ADDA | 1.000 | 0.995 | 0.001 | 0.001 | 0.002 |
| DAN | 1.000 | 1.000 | 0.001 | 0.001 | 0.001 |
| DANN | 0.001 | 0.903 | 0.001 | 0.001 | 0.001 |
| DeepCORAL | 0.001 | 1.000 | 0.007 | 0.998 | 1.000 |
| DeepJDOT | 1.000 | 1.000 | 0.246 | 1.000 | 1.000 |
| MeanTeacher | 1.000 | 1.000 | 0.216 | 1.000 | 1.000 |
| SimCLR | 1.000 | 1.000 | 0.001 | 1.000 | 0.999 |

(b) Scenario: sim-to-real (LaBr₃). Statistical significance tests compare testing accuracy (UDA > source-only).

| | MLP | CNN | TBNN (Li <i>et al.</i>) | TBNN-LinEmb | TBNN-NonlinEmb |
|-------------|--------------|--------------|--------------------------|--------------|----------------|
| ADDA | 0.001 | 0.001 | 0.001 | 0.002 | 0.001 |
| DAN | 0.001 | 0.002 | 0.001 | 0.001 | 0.001 |
| DANN | 0.001 | 0.001 | 0.001 | 0.001 | 0.001 |
| DeepCORAL | 0.001 | 0.001 | 0.001 | 0.001 | 0.001 |
| DeepJDOT | 0.042 | 0.010 | 0.005 | 0.001 | 0.001 |
| MeanTeacher | 0.001 | 0.976 | 0.001 | 0.968 | 0.014 |
| SimCLR | 0.001 | 0.001 | 0.001 | 0.001 | 0.001 |

(c) Scenario: sim-to-real (NaI(Tl)). Statistical significance tests compare testing accuracy (UDA > source-only).

| | MLP | CNN | TBNN (Li <i>et al.</i>) | TBNN-LinEmb | TBNN-NonlinEmb |
|-------------|--------------|--------------|--------------------------|--------------|----------------|
| ADDA | 0.001 | 0.065 | 0.001 | 0.001 | 0.500 |
| DAN | 0.001 | 0.188 | 0.001 | 0.001 | 0.001 |
| DANN | 0.001 | 0.024 | 0.001 | 0.001 | 0.001 |
| DeepCORAL | 0.001 | 0.001 | 0.001 | 0.001 | 0.001 |
| DeepJDOT | 0.001 | 0.884 | 0.001 | 0.001 | 0.001 |
| MeanTeacher | 0.991 | 0.999 | 0.001 | 0.019 | 0.001 |
| SimCLR | 0.001 | 0.003 | 0.001 | 0.001 | 0.001 |